Bioactive Materials 42 (2024) 550–572

Contents lists available at ScienceDirect

Bioactive Materials

journal homepage: www.keaipublishing.com/en/journals/bioactive-materials

Highly plastic Zn-0.3Ca alloy for guided bone regeneration membrane: Breaking the trade-off between antibacterial ability and biocompatibility

Xiang-Min Li [a], Zhang-Zhi Shi [a,b,**], Ayisulu Tuoliken [a], Wei Gou [a], Chang-Heng Li [a], Lu-Ning Wang [a,b,*]

[a] Beijing Advanced Innovation Center for Materials Genome Engineering, State Key Laboratory for Advance Metals and Materials, School of Materials Science and Engineering, University of Science and Technology Beijing, Beijing, 100083, China
[b] Institute of Materials Intelligent Technology, Liaoning Academy of Materials, Shenyang, 110004, China

ARTICLE INFO

Keywords:
Biodegradable Zn alloys
Second phase refinement
High plasticity
Antibacterial ability
Biocompatibility

ABSTRACT

A common problem for Zn alloys is the trade-off between antibacterial ability and biocompatibility. This paper proposes a strategy to solve this problem by increasing release ratio of Ca^{2+} ions, which is realized by significant refinement of $CaZn_{13}$ particles through bottom circulating water-cooled casting (BCWC) and rolling. Compared with conventionally fabricated Zn-0.3Ca alloy, the BCWC-rolled alloy shows higher antibacterial abilities against *E. coli* and *S. aureus*, meanwhile much less toxicity to MC3T3-E1 cells. Additionally, plasticity, degradation uniformity, and ability to induce osteogenic differentiation *in vitro* of the alloy are improved. The elongation up to 49 %, which is the highest among Zn alloys with Ca, and is achieved since the sizes of $CaZn_{13}$ particles and Zn grains are small and close. As a result, the long-standing problem of low formability of Zn alloys containing Ca has also been solved due to the elimination of large $CaZn_{13}$ particles. The BCWC-rolled alloy is a promising candidate of making GBR membrane.

1. Introduction

Guided bone regeneration (GBR) technology utilizes a GBR membrane to create a physical barrier between soft tissue and bone defects. This membrane selectively prevents fibroblasts from entering the bone defect, allowing osteoblasts to proliferate and facilitate bone regeneration. Therefore, it has been widely used in the fields of orthopedics and dentistry. It is one of the most effective methods to achieve bone defect repair [1–4]. The ideal GBR membrane should have good ductility while maintaining a certain level of strength, which is necessary to provide adequate support and effective shielding for the reconstruction of bone tissue function [5,6]. In addition, the ideal GBR membrane should also have an appropriate degradation rate, good antibacterial activity and good biocompatibility [7,8]. However, GBR membranes made of pure Ti are increasingly unable to meet the needs of patients due to the lack of biodegradability and thus require secondary surgical removal [9,10]. Bioabsorbable membranes, such as collagen, polylactic acid (PLA), and other biodegradable polymers, have been widely used as soft tissue barriers for GBR. However, they face challenges of inadequate mechanical properties, rapid degradation, limited osteogenic induction ability, and a lack of antibacterial ability [11–14].

Zn and its alloys have appropriate degradation rates, potential osteogenic and antibacterial activities, which show great potential for clinical transformation in the application of GBR membranes [15–17]. The strong antibacterial ability of Zn is attributed to its ability to easily bind with the negatively charged bacterial membrane, resulting in inactivation of bacteria [18]. Studies have shown that the minimum inhibitory concentration of Zn^{2+} on *S. aureus* is 9 μg/mL [19,20]. And the higher concentration of Zn^{2+}, the more pronounced of antibacterial effect [19,21].

However, potential cytotoxicity of Zn^{2+} cannot be ignored. It is found that the tolerance limit of human aortic smooth muscle cells (HASMC) to Zn^{2+} is 5.2 μg/mL [22]. The maximum Zn^{2+} tolerance of human dermal fibroblasts (HDF) is 3.5 μg/mL [23]. The tolerance limit

Peer review under responsibility of KeAi Communications Co., Ltd.
* Corresponding author. Beijing Advanced Innovation Center for Materials Genome Engineering, State Key Laboratory for Advance Metals and Materials, School of Materials Science and Engineering, University of Science and Technology Beijing, Beijing, 100083, China.
** Corresponding author. Beijing Advanced Innovation Center for Materials Genome Engineering, State Key Laboratory for Advance Metals and Materials, School of Materials Science and Engineering, University of Science and Technology Beijing, Beijing, 100083, China.
E-mail addresses: ryansterne@163.com (Z.-Z. Shi), luning.wang@ustb.edu.cn (L.-N. Wang).

https://doi.org/10.1016/j.bioactmat.2024.08.049
Received 28 January 2024; Received in revised form 21 July 2024; Accepted 31 August 2024

of human coronary artery endothelial cells (HCAEC) to Zn^{2+} is 6.5 μg/mL. When the concentration of Zn^{2+} exceeds 6.5 μg/mL, cell adhesion and proliferation activity are significantly reduced [24]. High concentrations of Zn^{2+} (14.4 ± 1.5 μg/mL) can impair the viability of mouse embryonic osteoblasts (MC3T3-E1) cells [17]. Ito et al. [25] reported that the release concentration of Zn^{2+} at 3 μg/mL in the cell culture medium is non-cytotoxic. However, this concentration is far below the minimum inhibitory concentration for *S. aureus*. At present, concentrations of Zn^{2+} in 100 % extract of Zn alloys are 10–25 μg/mL, which show good antibacterial effects, but are potentially toxic to the above mentioned cells [26]. Therefore, it is challenge to achieve synergistic improvement of antibacterial ability and biocompatibility.

Adding nutrient element Ca into Zn may have a chance to meet this challenge. As one of the main components of human bones, Ca positively promotes bone growth and wound healing [27]. Adding Ca to Zn for alloying can improve the bone regeneration process around the implant, promote the proliferation and differentiation of osteoblasts, and help enhance biocompatibilities of Zn alloys [28]. However, Zn-Ca alloys prepared by conventional casting methods, such as gravity casting, promote release of Zn^{2+} during immersion, which deteriorates cell viability and diminishes the gain effect of Ca [29,30].

Such a problem is mainly due to easy formation of coarse $CaZn_{13}$ second phase particles. A small amount of Ca addition will result in the formation of considerable volume fraction of coarse and hard $CaZn_{13}$ particles [31,32]. Moreover, some of the particles have a dendritic morphology and can grow longer than 100 μm. These particles act as cracking sources during plastic deformation and significantly reduce plasticity of Zn alloys [33]. For example, elongation to failure (EL) of as-cast Zn-1Ca alloy is only 2 % [29]. Even after subsequent extrusion, the EL can only increase to 8 %. Galvanic corrosion between the coarse $CaZn_{13}$ particles and the Zn matrix can lead to severe localized corrosion [30,34].

This paper solved the problem of coarse $CaZn_{13}$ particles. The microstructure, mechanical properties, *in vitro* degradation behavior, cytotoxicity, osteogenesis, and antibacterial ability of Zn-0.3Ca alloy are compared before and after refinement of $CaZn_{13}$ particles. It has been found that the refinement of Zn-0.3Ca alloy breaks the tradeoff between antibacterial and cytotoxicity, and enhances osteogenic properties *in vitro*.

2. Materials and methods

2.1. Alloy preparation

As shown in Fig. 1, a nominal composition of Zn-0.3Ca alloy sheet with a thickness of 0.8 mm was prepared using two different process routes. Route 1 (R1) was traditional casting, hot rolling and then cold rolling. Route 2 (R2) was bottom circulating water-cooled casting (BCWC), hot rolling, and then cold rolling. Through inductively coupled plasma atomic emission spectrometry (ICP-AES, Leeman Labs, USA), actual compositions of the alloys prepared by Route 1 and Route 2 were Zn-0.34Ca and Zn-0.36Ca, respectively. For convenience, they are designated afterwards as Zn03Ca (R1) and Zn03Ca (R2), respectively.

The traditional casting process was as follows: (1) Pure Zn (99.995 wt%) and Ca (99.99 wt%) were melted in a ZG-0.01 vacuum induction furnace. (2) Kept at 650 °C for 10 min (3) Cast into graphite mold, size φ80 × 100 mm. (4) Finally, it was air-cooled to room temperature. The cooling rate was about 8 °C/min. Then, a block measuring 50 × 50 × 10 mm was cut from the ingot for rolling.

BCWC casting process was as follows: (1) and (2) were the same as the above process; (3) Poured the melt was poured into an Al_2O_3 mold with a size of 50 × 50 × 10 mm. The base of the mold was made of pure Cu. The circulating coolant used was a mixture of liquid nitrogen and anhydrous ethanol at −20 °C, which played a directional and rapidly cooling effect. (4) After solidification, the ingot was quenched in ice water at 0 °C to restrict the further growth of Zn grains. (5) Finally, a 50 × 50 × 10 mm ingot was obtained for subsequent rolling.

The cooling rate of the alloy was measured by the contact thermocouple thermometer model TA612C. After pouring the alloy's liquid metal into the mold, the thermocouple probe was inserted into the liquid metal to monitor temperature changes during the cooling process. Temperature data was recorded at an interval of 1 s, within a range of 550 °C–30 °C. The cooling rate of BCWC was measured to be 390 °C/min, while that of the conventional casting was only about 8 °C/min.

The rolling processes of Zn03Ca (R1) and Zn03Ca (R2) were the same. The ingots were first held at 350 °C for 30 min, then hot rolled. After every 4 passes of rolling, the plates were shortly annealed at 350 °C for 5 min. After 16 passes of hot rolling, the plates were rolled to 5 mm in thickness. Then the plates were cold rolled to 0.8 mm in thickness. The total reduction of hot rolling and cold rolling reached 92 %. The thickness reduction per pass was the same for the two materials.

Samples with a diameter of 10 mm and a thickness of 0.5 mm were cut from the above two alloy plates. These samples were first polished with 600~7000 # sandpaper. Then polish the surface with 0.5 μm diamond paste until without scratches. Surface roughness (R_a) values of the two alloys are 0.16 μm and 0.18 μm (Fig. S2), respectively. They were stored under vacuum for subsequent degradation, antimicrobial and cell experiments.

2.2. Testing of mechanical properties

The tensile samples were designed according to the standard EN ISO

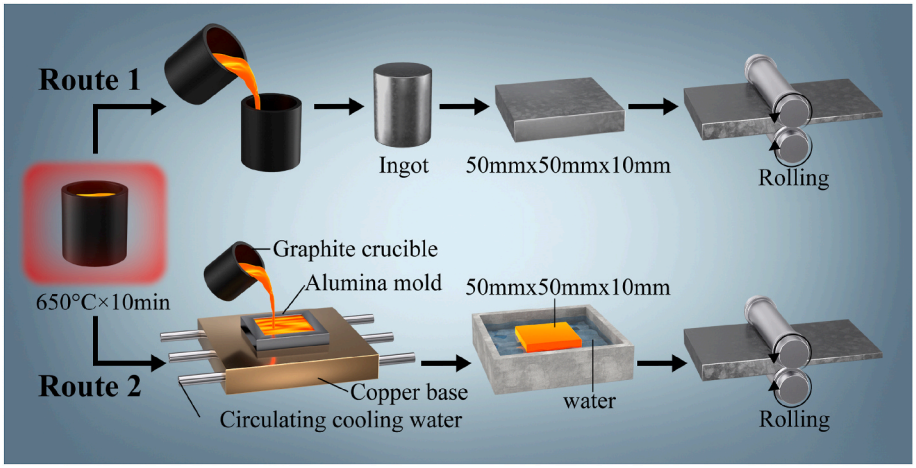

Fig. 1. A sketch of two processing routes. Route 1 (R1): conventional casting and then rolling. Route 2 (R2): BCWC and then rolling.

6892-1: 2009. The tensile direction was parallel to the direction of rolling. Room temperature tensile mechanical properties was tested by using Universal Testing Machine (CMT4105) with a strain rate of 1.4×10^{-3}/s. 4 parallel samples were tested. Hardness was tested by using a Vickers hardness tester (HV1000) with a load of 10 g and holding time of 10 s. Hardness values at five locations were measured and then averaged.

2.3. Microstructure characterization

The alloy samples were polished using sandpaper and diamond polishing paste to a scratch-free surface. They were then etched using a solution of 4 % nitric acid in alcohol. Microstructure was observed using an optical microscope (BX53M, OLYMPUS, Japan) equipped with a polarized light (PL) device. Microstructure was also examined using a scanning electron microscope (SEM) equipped with an electron backscatter diffraction (EBSD) camera (TESCAN MIRA3 LMH). The step size of the EBSD measurement was set to be 0.1 μm, suitable for fine grains. Another SEM (LEO 1450, LEO, Germany) equipped with Energy Dispersive Spectroscopy (EDS) probe was used to analyze corrosion products and surface morphology.

2.4. Electrochemical and immersion tests

The alloy was electrochemically tested in a standard three-electrode system using an electrochemical workstation (ModuLab XM, Ametek, UK). The test temperature was 37 °C, the electrolyte solution was normal saline (0.9 % NaCl solution), and the solution volume was 150 mL. The reference electrode was a saturated calomel electrode (SCE), the auxiliary electrode was a platinum sheet, and a sample of alloy was used as the working electrode. Open circuit potential (OCP) test was carried out for 30 min before conducting the electrochemical impedance spectroscopy (EIS), and potentiodynamic polarization (PDP) tests, in order to stabilize the sample surface. PDP tests were conducted in a range of −0.3 V *vs.* OCP to −0.7 V *vs.* SCE, at a constant scan rate of 1 mV/s. The measured data was processed using ModuLab XM Studio ECS. Furthermore, impedance spectrum data were fitted using ZSimpWin software. The self-corrosion potential and corrosion current of the alloy were obtained using the Tafel extrapolation method. According to the standard ASTM-G102-89, the corrosion rate of the alloy was calculated using Faraday's law [35].

To accurately evaluate the release of Ca^{2+} ions in Zn-Ca alloy, 0.9 % NaCl solution was used as the corrosion medium for the immersion tests. The test was conducted in accordance with the ASTM-G31-72 standard, and the ratio of solution volume to sample area was greater than 20 mL/cm^2. The soaking process was carried out in a constant temperature incubator, and the solution was refreshed every 48 h. Once the soaking time period was completed, the sample was removed from the solution and carefully washed with deionized water. The samples used to observe the corrosion products were directly placed in the drying box and dried at 37 °C for 24 h. For weight loss measurement, the corrosion products were removed with 100 g/L NH_4Cl solution at 70 °C, following the standard ASTM G1-90. Then, the samples were rinsed with deionized water and dried at 37 °C for 24 h. The immersion corrosion rate was calculated according to the standard ASTM-G31-72, as described in a previously published paper [35].

2.5. Antibacterial examination

Based on DIN EN ISO 20645-2004, the antibacterial properties of Zn-0.3Ca alloy against Escherichia coli (*E. coli*, ATCC25922, China) and Staphylococcus aureus (S. aureus, CMCC26003, China) were evaluated using the agar plate diffusion method and the sample and bacteria co-culture method.

The agar plate diffusion method involved evenly spreading a bacterial suspension with a concentration of 1×10^8 CFU/mL on the surface of an agar culture dish. The dish was then sterilized on a sterile table for 30 min using ultraviolet light. The round alloy samples were placed in the center of the agar plate and incubated at 37 °C for 24 h to observe and measure the diameter of inhibition zone (*IZD*). *IZD* > 1 mm indicates that the alloy has a significant antibacterial effect [36]. Ti6Al4V alloy was used as the control group. At least 3 parallel samples were tested for statistical analysis.

The sample and bacteria co-culture method involved placing the alloy discs in a 24-well plate, adding a sample to each well, and then adding 2 mL of bacterial suspension with a concentration of 1×10^5 CFU/mL. After incubating the alloy samples in a shaker at 37 °C for 24 h, removed them and measure the absorbance in the bacterial suspension using a spectrophotometer (UNIC-7200, China). Antibacterial properties of the materials were evaluated based on the optical density (*OD*) value in the bacterial suspension. In order to minimize experimental error, three parallel samples were prepared for each alloy. A well plate with 2 mL bacterial suspension but no alloy sample was established as the blank control group.

The alloy samples mentioned above were taken from the bacterial fluids, washed three times with a PBS buffer solution to remove non-adherent bacteria from surface. Then, the left bacteria were fixed, dehydrated, dried, and sprayed with gold. Morphologies of the bacteria on sample surfaces were observed by SEM.

2.6. Cytotoxicity tests and osteogenic differentiation

2.6.1. Preparation of alloy extract

The samples (10 mm in diameter, 0.5 mm in thickness) were cleaned and sterilized. Then, they were immersed in α-medium, i.e., α-MEM, 10 % fetal bovine serum (FBS), 100 U/mL penicillin, and 100 μg/mL streptomycin, with a surface area to medium ratio of 1.25 mL/cm^2 (according to ISO 10993–5:2009). They were placed in an atmosphere of 37 °C, 95 % humidity and 5 % CO_2 for 72 h to make an extract of 100 % concentration. Subsequently, the concentration of extract was diluted to 75 %, 50 % and 25 %, then refrigerated at 4 °C. Ionic concentration of the 100 % extract was detected using inductively coupled plasma atomic emission spectroscopy (ICP-AES).

2.6.2. Cell morphology and proliferation viability

Mouse embryo osteoblast precursor (MC3T3-E1) cells were used to assess cell viability. Firstly, cell suspension was prepared by centrifugation following trypsin digestion. According to the protocol, 100 μL (2×10^4 cells/mL) of cell suspension was added to each well of a 96-well plate. The cells were then incubated in a cell incubator with 95 % humidity and 5 % CO_2 for 24 h. Once the cells adhered to the plate, the original medium in each well was replaced with 25~100 % concentrations of the extract medium. The control group was cultured with normal medium without the extract. Each extract concentration was placed in four parallel wells with the extract refreshed every other day. The cells were cultured at 37 °C with 5 % CO_2 and 95 % humidity for 1 day and 3 days. Cell viability was measured using the CCK-8 assay [37]. The formula is (1):

$$CV = (OD_e - OD_b) / (OD_c - OD_b) \times 100\%, \quad (1)$$

where *CV* represents cell survival rate, OD_e represents the absorbance of an experimental group with the extract and the cells, OD_b represents the absorbance of the negative control group without cells nor the extract, and OD_c represents the absorbance of the positive control group with cells but no extract.

After 1 day and 3 days of culture, cell morphology was observed using an inverted fluorescence microscope (Zeiss Axio Vert A1, Germany). MC3T3-E1 cells cultured in 25~100 % extracts were stained with calcein-AM/PI live/dead staining reagent for 20 min. After removing the staining solution, the cells were washed twice with phosphate buffer solution (PBS). Then, 100 μL of PBS buffer was added

to each well for cell morphology observation. The living cells appeared green, while the dead cells appeared red. In order to further observe the morphology of cell adhesion, the cells were stained with Phalloidin-TRITC (Sigma) and 4′,6-Diamidino-2-phenylindole dihydrochloride (DAPI, Sigma) to visualize their cytoskeleton and nucleus using laser scanning confocal microscopy (CLSM, Leica TCS SP2, Heidelberg, Germany).

2.6.3. Osteogenic differentiation in vitro

Osteogenic differentiation ability of the cells induced by the extract was evaluated using Alizarin Red S (ARS) staining and an alkaline phosphatase (ALP) activity assay. The resuspended cells were added to a 24-well plate at a density of 3×10^4 cells per well. The cell culture and extract replacement methods used were consistent with the CCK-8 method described above. After 7 and 14 days of culture in various concentrations of extract and normal medium, the ALP activity of MC3T3-E1 cells was quantitatively measured using an alkaline phosphatase (ALP/AKP) detection kit. The *OD* value at 520 nm was then measured using a multifunctional microplate reader. The qualitative detection of ALP was performed using the BCIP/NBT alkaline phosphatase kit. After 7 and 14 days of culture, the cells were fixed with 4 % paraformaldehyde, and the BCIP/NBT staining solution was added. After incubating at room temperature in darkness until color became apparent, the reaction was stopped and observed under an inverted fluorescence microscope. Dark blue or purple-blue indicates high ALP activity.

ARS staining was performed using the Alizarin Red S staining kit for osteogenesis, in order to analyze cells cultured for 7 and 14 days in 25~50 % extracts and normal medium. The staining method was the same as the ALP activity detection mentioned above. The staining results were observed using an inverted fluorescence microscope. Orange-red color indicated that calcium deposition was evident and osteoblast differentiation was complete. After ARS staining, the staining solution in each well was removed, and 10 % cetane pyridine chloride was added. The samples were then incubated at room temperature in the dark for 30 min. The *OD* value at a wavelength of 562 nm was measured using a multifunctional microplate reader. The control group was cultured in a normal medium without any extract. Each group included at least three parallel samples for statistical analysis.

2.7. Statistical analysis

The data were expressed as mean ± standard deviation (SD). One-way analysis of variance (ANOVA) was used to evaluate the statistical significance of differences between groups using SPSS software (Version 17.0, SPSS Inc., USA). The difference between $^*p < 0.05$ and $^*p < 0.01$ was considered statistically significant and highly significant, respectively.

3. Results

3.1. Mechanical properties

For convenience, Zn-0.3Ca alloy in traditional cast, cast + rolled and BCWC + rolled states are designated as 'C', 'CR' and 'BR', respectively. It can be seen from Fig. 2a that Zn-0.3Ca (BR) exhibits a formability

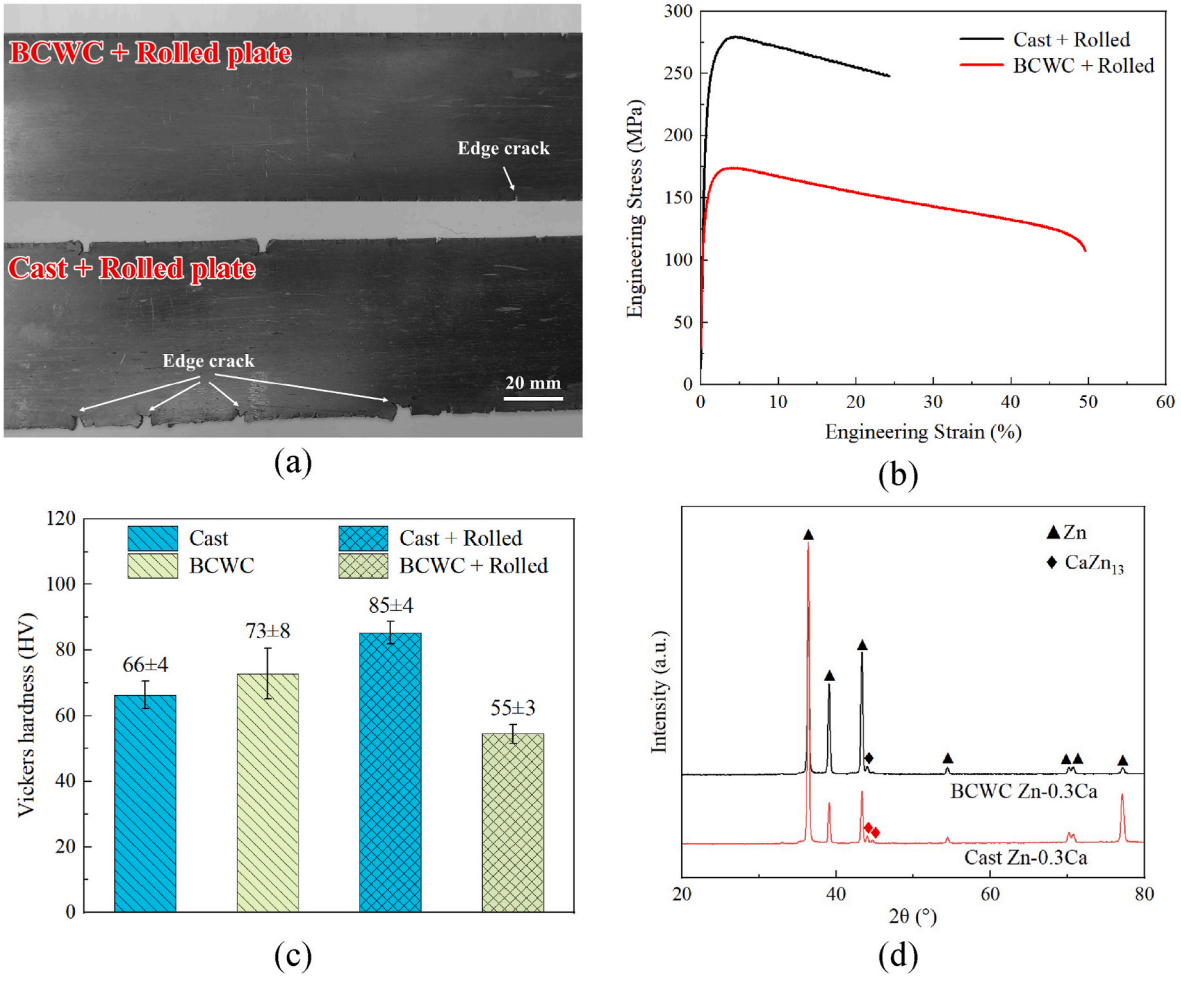

Fig. 2. Zn-0.3Ca alloy: (a) Rolled plates; (b) Tensile engineering stress-strain curves; (c) Distribution of hardness values; (d) XRD spectra.

superior to Zn-0.3Ca (CR). The latter one has many edge cracks. Fig. 2b shows engineering stress-strain curves of the alloys, with the corresponding data listed in Table 1. Zn-0.3Ca (CR) exhibits yield strength (YS) of 222 ± 23 MPa, the ultimate tensile strength (UTS) of 275 ± 5 MPa, and EL of 25 ± 1 %. By contrast, Zn-0.3Ca (BR) exhibits YS of 146 ± 4 MPa, UTS of 174 ± 1 MPa, and EL of 49 ± 4 %. Notably, the YS of Zn-0.3Ca (BR) remains significantly higher than that of the extruded Zn-0.4Ca alloy reported in previous literature [26]. Additionally, the YS of Zn-0.3Ca (BR) is much higher than that of pure Mg and pure Zn GBR membranes implanted in animal trials, which typically exhibit YS values of less than 100 MPa [17,38]. This indicates that Zn-0.3Ca (BR) can provide sufficient mechanical support in applications.

Fig. 2c shows hardness values distribution of Zn-0.3Ca alloys. The hardness of Zn-0.3Ca (C) is 66 HV, which increases to 85 HV after rolling, approximately 22 % higher than those before rolling. The hardness of Zn-0.3Ca (BCWC) is 73 HV, which decreases to 52 HV after rolling. Zn-0.3Ca (BR) is the softest and the most flexible (Fig. 2c and b), which is favorable for GBR membranes. When a GBR membrane contact with soft tissue, excessive strength and hardness can lead to reduced biological suitability and potential harm to the soft tissue [13,17].

3.2. Microstructures

Fig. 2d shows that BCWC does not alter the phase constitution of Zn-0.3Ca alloy, i.e., Zn (structure with lattice parameters of $a = 0.2665$ nm and $c = 0.4947$ nm [31]) and $CaZn_{13}$ ($a = 1.213$ nm [33]). However, {0001} diffraction peaks of Zn are significantly decreased after BCWC, indicating a weakened basal texture. Fig. 3a shows Zn grains of Zn-0.3Ca (C) alloy. where most of the grains are equiaxed and relatively coarse, with an average grain size of 352 ± 45 μm. After BCWC, the grains are refined to an average size of 157 ± 14 μm (Fig. 3b).

As shown in Fig. 3c, $CaZn_{13}$ particles in Zn-0.3Ca (C) alloy have two shapes: granular and long dendritic. The formation of long dendrites is due to the slow cooling rate of the alloy melt in traditional casting. The average size (in equivalent diameter) of all the $CaZn_{13}$ particles is 65.0 ± 5.4 μm. After BCWC (Fig. 3d), $CaZn_{13}$ particles are significantly refined and more uniformly distributed, which eliminates the long $CaZn_{13}$ dendrites.

In the BCWC ingot, $CaZn_{13}$ particles exhibit similar sizes and distributions from top to bottom (Fig. 3d). which indicates the cooling rate varies little in depth. The average sizes (in equivalent diameter) of $CaZn_{13}$ particles are 6.8 ± 1.7 μm, 6.7 ± 1.9 μm, and 6.5 ± 1.3 μm from top to bottom, respectively. The average of the three sizes, i.e., 6.7 ± 1.6 μm, can describe the size of $CaZn_{13}$ particles in Zn-0.3Ca (BCWC) well (Fig. 4f). Compared to the traditional casting, $CaZn_{13}$ particles are refined by 90 % approximately (Fig. 4f). Fig. 4a and b shows microstructures of Zn-0.3Ca (CR) and Zn-0.3Ca (BR) after rolling, respectively. $CaZn_{13}$ particles distribute along the rolling direction (RD). $CaZn_{13}$ particles exhibit similar sizes and distributions from top to bottom (Fig. S1). The average size of $CaZn_{13}$ particles in Zn-0.3Ca (CR) is 10.8 ± 4.3 μm, while that in Zn-0.3Ca (BR) is only 2.1 ± 1.1 μm, i.e., a refinement by about 81 % (Fig. 4f). The fraction of $CaZn_{13}$ particles in Zn-0.3Ca (CR) and Zn-0.3Ca (BR) are measured to be 8.07 % and 8.22 %, respectively (Fig. 4f).

The SEM and EDS analysis of the microstructures of Zn-0.3Ca (CR) and Zn-0.3Ca (BR) are shown in Fig. 4c and d, respectively. Only Zn and $CaZn_{13}$ phases are present in the alloy, which is consistent with the XRD results. EDS results indicate that the Ca element in Zn-0.3Ca (CR) exists in $CaZn_{13}$ particles, while a limited portion (i.e., 0.4 at.%) of Ca element in Zn-0.3Ca (BR) is dissolved into the Zn matrix, as shown in position 1 in Fig. 4d. This is due to the fast cooling rate of BCWC.

Table 1
Tensile mechanical properties of Zn-0.3Ca alloys.

State	YS (MPa)	UTS (MPa)	EL (%)
Cast + Rolled	222 ± 23	275 ± 5	25 ± 1
BCWC + Rolled	146 ± 4	174 ± 1	49 ± 4

EBSD maps of Zn-0.3Ca (CR) are shown in Fig. 5. It can be seen from the inversed pole figure (IPF) colored map in Fig. 5a that there are large and small Zn grains, some of the small grains are formed around $CaZn_{13}$ particles due to particle-stimulated nucleation (PSN) effect. The large grains are elongated along the RD, indicating that they are not recrystallized. The average grain size of Zn grains in Zn-0.3Ca (CR) is 3.1 ± 1.5 μm (Fig. 4e), and the percentage of grains that larger than 4 μm accounting for 14.2 % (Fig. 5c). By contrast, the uniformity of Zn grain sizes is obviously improved in Zn-0.3Ca (BR), as shown in the IPF-colored map in Fig. 5b. The average size of Zn grains is 1.4 ± 0.8 μm (Fig. 4e), and the percentage of grains larger that than 4 μm is only 5.7 % (Fig. 5d), which is much lower than that of Zn-0.3Ca (CR). {10–12}<-1011> deformation twins form in some Zn grains, as shown in the grain boundary (GB) maps in Fig. 5e and f. This type of twin is general in HCP structured metals including various Zn alloys [33,39].

Kernel average misorientation (KAM) map of Zn-0.3Ca (CR) is shown in Fig. 6a. There are band-like regions with high dislocation densities in bright and warm colors. By contrast, BCWC refines and evenly distributes $CaZn_{13}$ particles, resulting in a more uniform recrystallization of Zn grains, as shown in the KAM map in Fig. 6b. A KAM value less than 1° indicates recrystallization [40]. More than 90 % of the Zn grains in Zn-0.3Ca (BR) have recrystallized (Fig. 6e), while that is 70 % in Zn-0.3Ca (CR) (Fig. 6e). In both the alloys, all the $CaZn_{13}$ particles have KAM values < 1°, indicating that these hard particles are little deformed during rolling.

The grain orientation spread (GOS) can be utilized for the identification of original deformed and recrystallized grains [41,42]. According to previous studies [43–45], different GOS values define completely recrystallized grains (GOS <2°), partially recrystallized grains (2° < GOS <5°), and primitive deformed grains (GOS >5°) in the GOS map. Fig. 6c shows the GOS map of Zn-0.3Ca (CR). The large grain regions are bright in color and have high GOS values. Small grains around the large grains have low GOS values due to recrystallization. By contrast, most of the grains in Zn-0.3Ca (BR) are closer to the blue end and have lower GOS values, as shown in Fig. 6d. The distribution of the GOS values of the two alloys are shown in Fig. 6f. The proportion of grains with GOS <2° in Zn-0.3Ca (CR) and Zn-0.3Ca (BR) are 26.8 % and 60.3 %, respectively. The proportion of grains with 2° < GOS <5° are 41.4 % and 28.2 %, respectively. The proportion of grains with GOS >5° are 31.8 % and 11.5 %, respectively. By calculation, 68.2 % of the grains in Zn-0.3Ca (CR) are recrystallized, while the proportion of recrystallization in Zn-0.3Ca (BR) reaches 88.5 %. This indicates that the degree of recrystallization of Zn-0.3Ca (BR) is higher, which is consistent with the conclusion in KAM.

The Zn grains in both the Zn-0.3Ca (CR) and Zn-0.3Ca (BR) alloys exhibit a distinct rolling basal texture, featured with (0001) basal plane close to ND, as shown in Fig. 6g and h. This texture is formed due to crystal rotation that caused by {0001}<2-1-10> basal dislocation slipping [40]. It can also be seen from Fig. 5c that (0001) poles of a few Zn grains turn toward RD. This is due to a twinning crystal rotation of 86° [39]. The basal texture intensity of Zn-0.3Ca (CR) is 6.5 mrd (multiples of random distribution), while the basal texture intensity of Zn-0.3Ca (BR) is 5.2 mrd, indicating that the basal texture is weakened after BCWC and rolling.

3.3. In vitro corrosion behaviors

Fig. 7a shows electrochemical polarization curves of Zn-0.3Ca (CR) and Zn-0.3Ca (BR). There is no obvious difference in their corrosion potentials (E_{corr}). E_{corr} of Zn-0.3Ca (CR) is −1.06 ± 0.03 V, and that of Zn-0.3Ca (BR) is −1.09 ± 0.06 V (Table 2). However, the corrosion current density (I_{corr}) of Zn-0.3Ca (BR) is 7.81 ± 0.22 μA/cm^2, which is significantly higher than that of Zn-0.3Ca (CR) (5.95 ± 0.37 μA/cm^2). No passivation zone is found for both the alloys in their anodic branches,

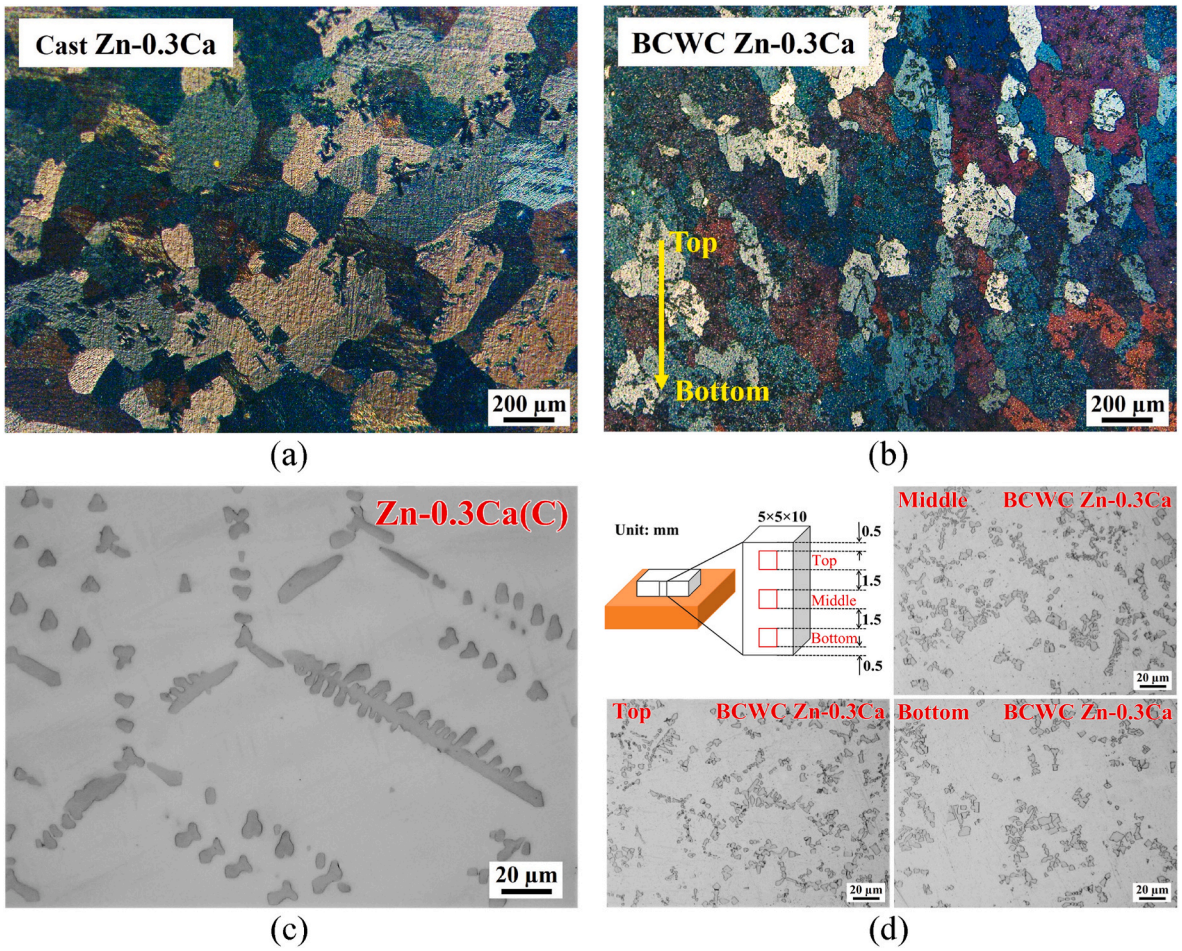

Fig. 3. Metallographs of Zn-0.3Ca alloy: (a) Traditional casting; (b) BCWC; $CaZn_{13}$ particles after traditional casting in (c), after BCWC in (d).

and the I_{corr} values increase rapidly between −1.0 V and −0.8 V (Fig. 7a). This may be due to further corrosion caused by breakdown of corrosion layer. The increase of I_{corr} results in an accelerated electrochemical corrosion rate (CR_e) of Zn-0.3Ca (BR), which is measured to be 192 ± 13 μm/y (Table 2).

Fig. 7b shows that the radius of the loop in the high frequency region of the impedance spectrum of Zn-0.3Ca (CR) is larger than that of Zn-0.3Ca (BR). In the simulation circuit, the Warburg diffusion element 'W' exhibits a 45° line in the low-frequency range. Similar simulation circuits are also applied in other biodegradable Zn alloys [46,47]. Additionally, Values of charge transfer resistance (R_{ct}) and corrosion product layer resistance (R_c) of Zn-0.3Ca (CR) are larger than those of Zn-0.3Ca (BR), as shown in Table 3, indicating a better corrosion resistance of Zn-0.3Ca (CR). From Fig. 7c, it can be seen that the highest phase angle of Zn-0.3Ca (CR) is more than 25° (Fig. 7c), which is significantly higher than Zn-0.3Ca (BR). This indicates that the corrosion layer in Zn-0.3Ca (CR) is relatively dense and slows down the corrosion process. This also suggests that the corrosion resistance of Zn-0.3Ca (BR) is inferior to that of Zn-0.3Ca (CR).

Fig. 7d shows corrosion rates (CR_i) of the alloys immersed in 0.9 % NaCl solution for 30 days. CR_i values of Zn-0.3Ca (CR) and Zn-0.3Ca (BR) are 127 ± 12 μm/y and 154 ± 21 μm/y, respectively. The corrosion rate of Zn-0.3Ca (BR) is 21 % higher than that of Zn-0.3Ca (CR), which is consistent with the electrochemical results.

Fig. 8a and b shows that after 30 days of immersion, surfaces of Zn-0.3Ca (CR) and Zn-0.3Ca (BR) samples are covered with thick and similar corrosion products. The morphology of the corrosion products is needle-like or spherical. EDS analysis shows that O content in acicular corrosion products is relatively high, as indicated by points a1 and a2 in Fig. 8a, and points b1 and b2 in Fig. 8b. The concentration of Cl element in the spherical corrosion product increases, as indicated by points a3 in Fig. 8a, and points b3 in Fig. 8b. Functional groups of OH^-, H_2O, Cl^-, CO_3^{2-} and ZnO are identified in the corrosion products by using FTIR spectroscopy (Fig. 8c).

XPS spectra in Fig. 8d shows that the main chemical elements in the corrosion products of both alloys are Zn, C, O and Cl. The $Zn2p_{3/2}$ spectrum of Zn-0.3Ca (CR) is shown in Fig. 8e and that of Zn-0.3Ca (BR) is shown in Fig. 8f. The strongest diffraction peak with a binding energy of 1022.26 eV is mainly attributed to the presence of ZnO and $Zn(OH)_2$ [48]. Previous studies have shown that the diffraction peak at 1023.2 e V corresponds to $Zn_5(OH)_8Cl_2{\cdot}H_2O$ [49–51].

After 3 days' immersion, significant difference can be observed in surface morphologies of the two alloys after removal of the corrosion products. Severe pitting is observed on the surface of Zn-0.3Ca (CR) (Fig. 9a). Large corrosion pits with an average size of about 100 μm usually appear together with large $CaZn_{13}$ particles, as pointed out by points 2 and 3 in Fig. 9a. $CaZn_{13}$ acts as cathode in Zn-$CaZn_{13}$ galvanic cell. Corrosion pits on Zn-0.3Ca (BR) after 3 days' immersion are much smaller (i.e., <20 μm) and distribute more evenly (Fig. 9b). After 30 days' immersion, uneven corrosion of Zn-0.3Ca (CR) is further exacerbated. The corrosion pits continue to expand in diameter and in depth. One pit is enlarged in the figure, in which several $CaZn_{13}$ particles (as marked by points 2 and 3) aggregate at the bottom of the pit. By contrast, corrosion uniformity still high for Zn-0.3Ca (BR), as shown in Fig. 9d.

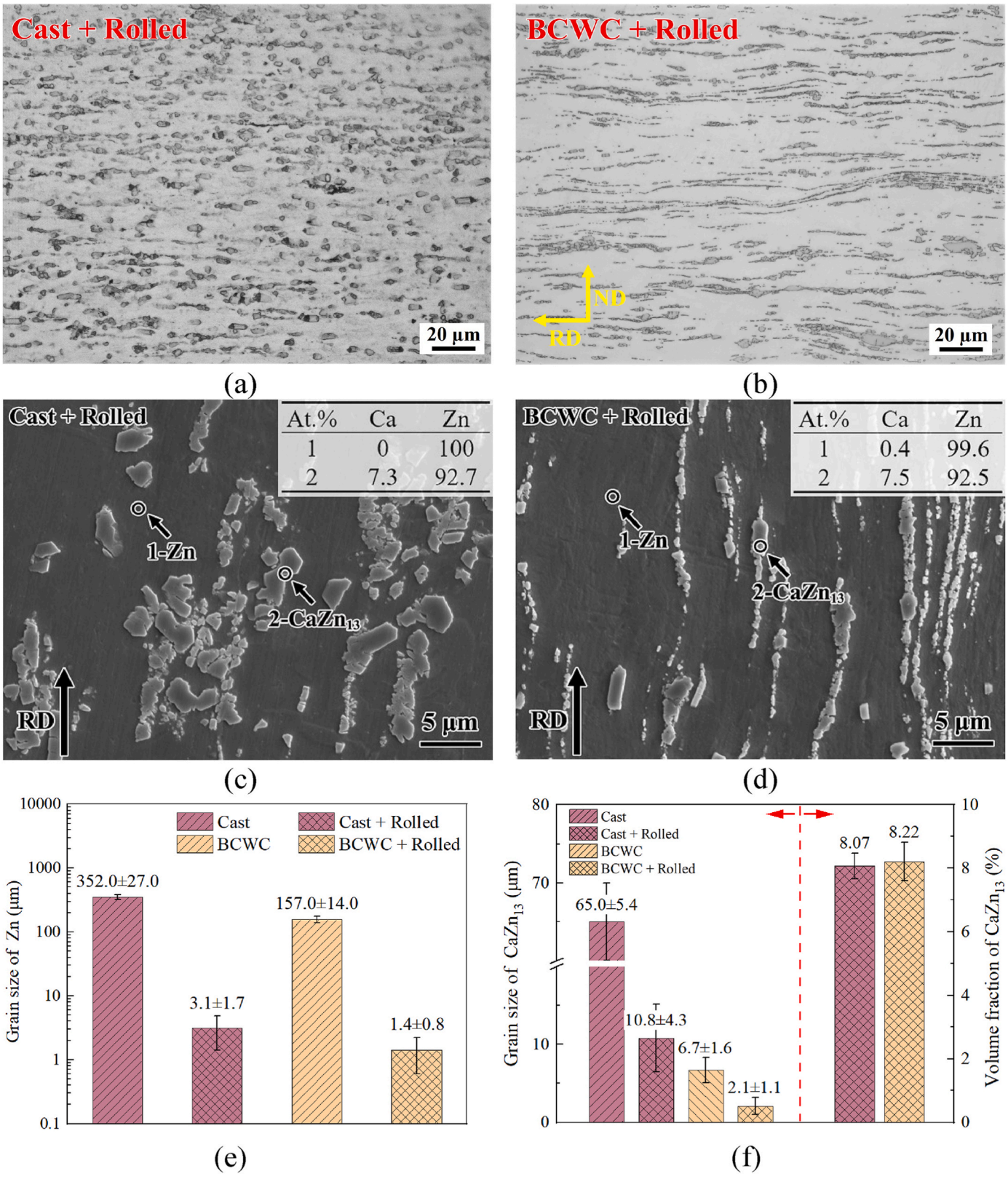

Fig. 4. $CaZn_{13}$ particles after cast-rolled in (a), and after BCWC-rolled in (b); Microstructures under SEM after cast-rolled in (c), and after BCWC-rolled in (d); (e) Grain size of Zn in four states; (f) Size and volume fractionin of $CaZn_{13}$ particles.

3.4. Antibacterial ability

The inhibition zone diameters (*IZDs*) of Zn-0.3Ca (CR) and Zn-0.3Ca (BR) against Escherichia coli (*E. coli*) and Staphylococcus aureus (*S. aureus*) are shown in Fig. 10. No bacteriostatic ring is observed around Ti6Al4V for *E. coli* and *S. aureus*, indicating that Ti6Al4V has no antibacterial ability. Both Zn alloys exhibit antibacterial ability against *E. coli* and *S. aureus*. Zn-0.3Ca (BR) has *IZDs* larger than those of Zn-

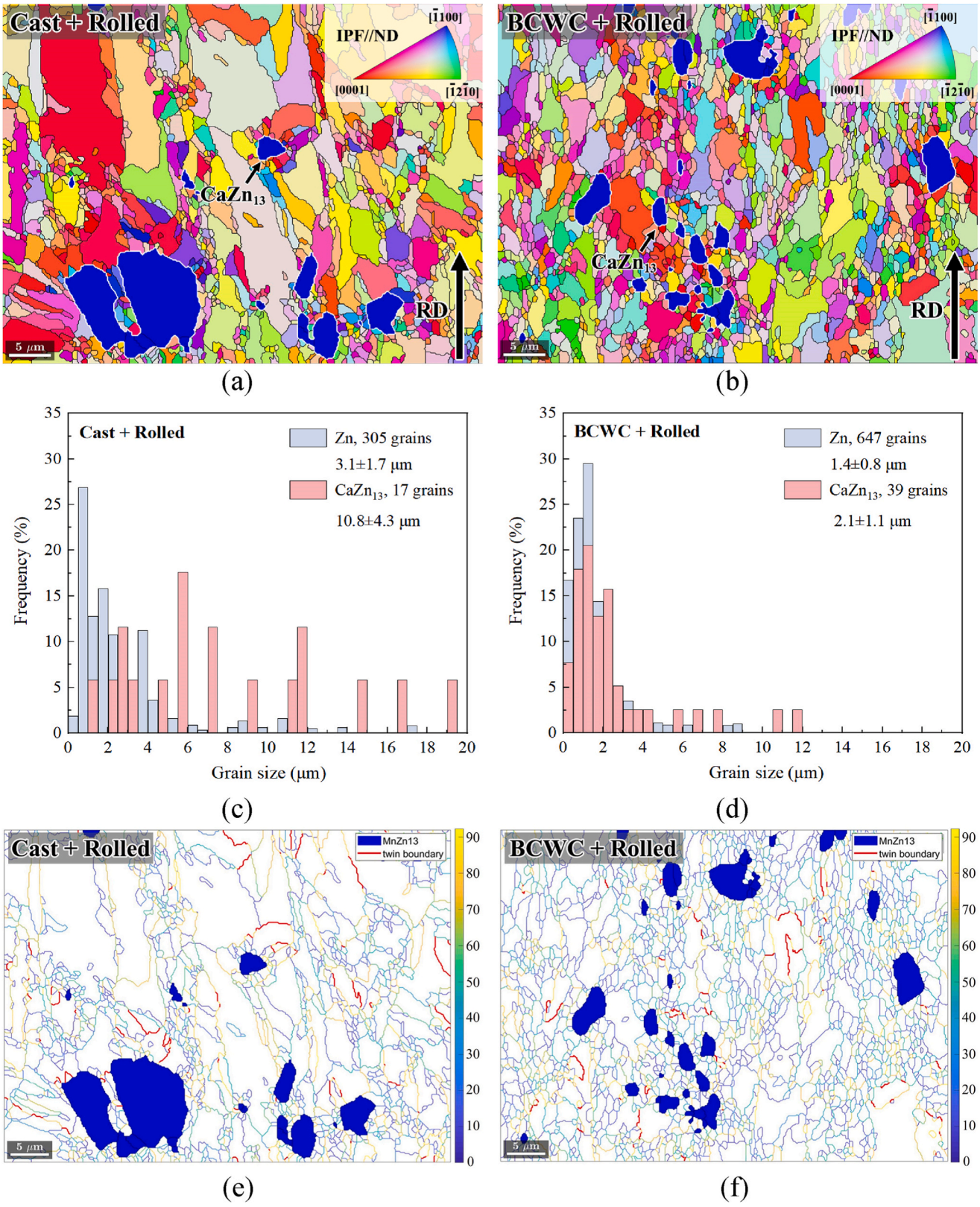

Fig. 5. EBSD maps of Zn-0.3Ca alloys: Inverse pole figure (IPF) colored maps of Zn-0.3Ca (CR) in (a) and Zn-0.3Ca (BR) in (b); Grain size distributions of Zn-0.3Ca (CR) in (c) and Zn-0.3Ca (BR) in (d); Grain boundary (GB) misorientation maps of Zn-0.3Ca (CR) in (e) and Zn-0.3Ca (BR) in (f). Zn grains in (a) and (b) are colored according to IPF, while $CaZn_{13}$ particles are in yellow. GBs with misorientations larger than 15° are outlined in black, and sub-GBs with misorientations larger than 5° are outlined in grey. The phase boundary between Zn and $CaZn_{13}$ is outlined in white in the IPF-colored maps. {10–12} twin boundaries are outlined in red in the GB maps.

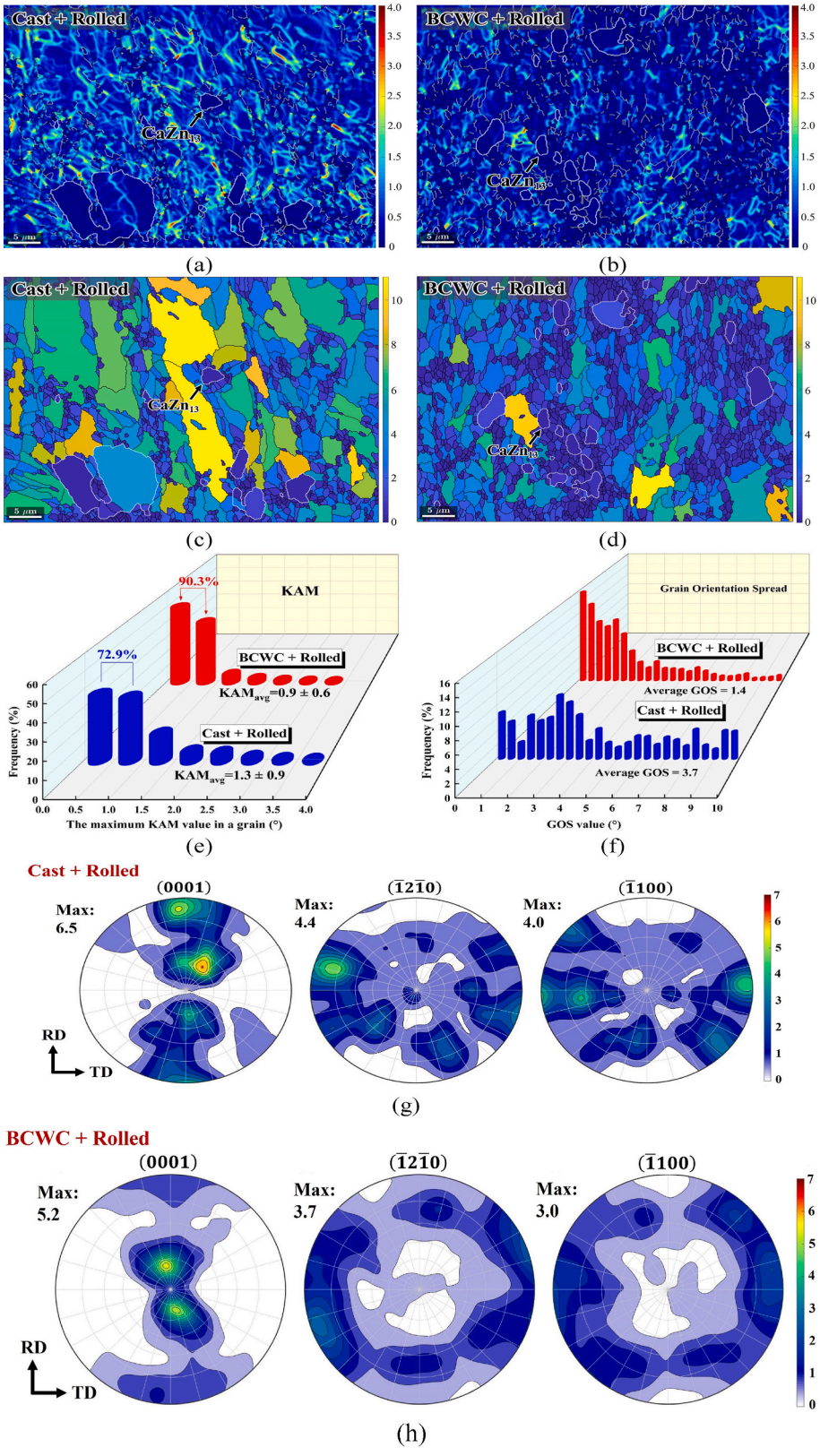

Fig. 6. Kernel average misorientation (KAM) maps of Zn-0.3Ca (CR) in (a) and Zn-0.3Ca (BR) in (b); Grain orientation spread (GOS) maps of Zn-0.3Ca (CR) in (c) and Zn-0.3Ca (BR) in (d); (e) Distributions of the maximum intragranular KAM values; (f) Distributions of the GOS values; Pole figures of Zn grains in Zn-0.3Ca (CR) in (g) and Zn-0.3Ca (BR) in (h).

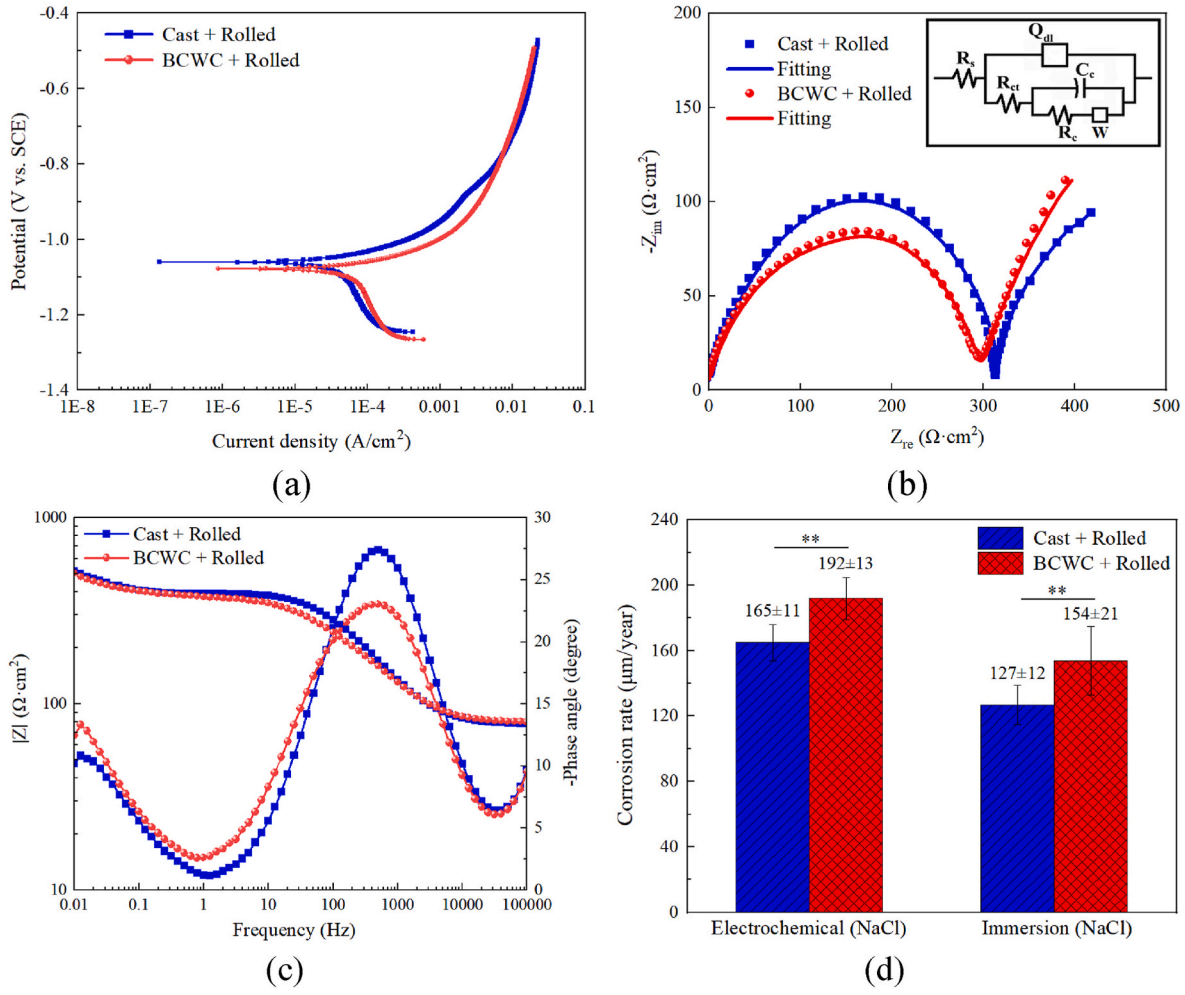

Fig. 7. Zn-0.3Ca alloys in 0.9 % NaCl (37 °C): (a) Polarization curves; (b) Nyquist plot; (c) Bode plots; (d) Corrosion rates.

Table 2
Polarization curve fitting and immersion corrosion rate of Zn-0.3Ca alloy. CR_e is corrosion rate measured from electrochemical test, while CR_i is that from immersion test.

State	E_{corr} (V)	I_{corr} (μA/cm²)	CR_e (μm/y)	CR_i (μm/y)
Cast + Rolled	−1.06 ± 0.03	5.95 ± 0.37	165 ± 11	127 ± 12
BCWC + Rolled	−1.09 ± 0.06	7.81 ± 0.22	192 ± 13	154 ± 21

0.3Ca (CR). *E. coli IZD* of Zn-0.3Ca (BR) is 2.44 ± 0.17 mm, which is about 1.3 times of that of Zn-0.3Ca (CR). *S. aureus IZD* of Zn-0.3Ca (BR) is 8.35 ± 1.36 mm, which is about 1.7 times of that of Zn-0.3Ca (CR). So, Zn-0.3Ca (BR) exhibits a much better antibacterial ability.

After co-culturing the alloy samples with *E. coli* and *S. aureus* in liquid agar broth for 24 h, *OD* values in the bacterial fluids are shown in Fig. 11a. The smaller the *OD* value, the higher transmittance, indicating that a lower bacterial concentration in the solution results in a stronger antibacterial effect. Zn-0.3Ca (BR) has the lowest *OD* values for *E. coli* and *S. aureus*, indicating its antibacterial ability is the best. Fig. 11b shows concentrations of Zn^{2+} and Ca^{2+} released in the bacterial fluid. The release of Zn^{2+} from Zn-0.3Ca (BR) in bacterial fluids of *E. coli* and *S. aureus* are about 7.6 % and 3.4 % lower than those of Zn-0.3Ca (CR), respectively. However, the amount of Ca^{2+} released from Zn-0.3Ca (BR) in bacterial fluids of *E. coli* and *S. aureus* are about 2.0 and 2.9 times of those from Zn-0.3Ca (CR), respectively.

Fig. 11c shows adhered *E. coli* bacteria on surfaces of Ti6Al4V and the Zn-Ca alloys. On the surfaces of the three alloys, *E. coli* bacteria show a rod-like morphology. Densities of the adhered *E. coli* bacteria are ranked as follows: Zn-0.3Ca (BR) < Zn-0.3Ca (CR) < Ti6Al4V. Fig. 11d shows adhered *S. aureus* bacteria on surfaces of the three alloys. On the surfaces of the three alloys, *S. aureus* bacteria show a spherical morphology with an average size about 1 μm. Similarly, densities of the adhered *S. aureus* bacteria are ranked as follows: Zn-0.3Ca (BR) < Zn-0.3Ca (CR) < Ti6Al4V.

Table 3
EIS fitting results of Zn-0.3Ca alloy.

State	R_s (Ω·cm²)	Q_{dl}		R_{ct} (Ω·cm²)	C_c (10^{-3}F/cm²)	R_c (Ω·cm²)	$W \times 10^{-4}$ (Ω cm² $S^{-0.5}$)
		$Y_0 \times 10^{-6}$ (Ω^{-1} cm^{-2} S^{-2})	n				
Cast + Rolled	74.5 ± 5.9	2.5 ± 1.1	0.8 ± 0.1	325.4 ± 11.2	18.4 ± 3.5	113.1 ± 5.4	33.6 ± 8.3
BCWC + Rolled	76.5 ± 3.6	6.2 ± 1.4	0.7 ± 0.3	219.5 ± 8.5	13.8 ± 1.2	71.8 ± 9.2	9.6 ± 2.4

Note: R_s: resistance of solution; R_{ct}: charge transfer resistance of alloy and solution; R_c: resistance of corrosion product layer; C_c: capacitance of corrosion product layer; Q_{dl}: constant phase element and electric double layer capacitance; *W*: Semi-infinite diffusion impedance.

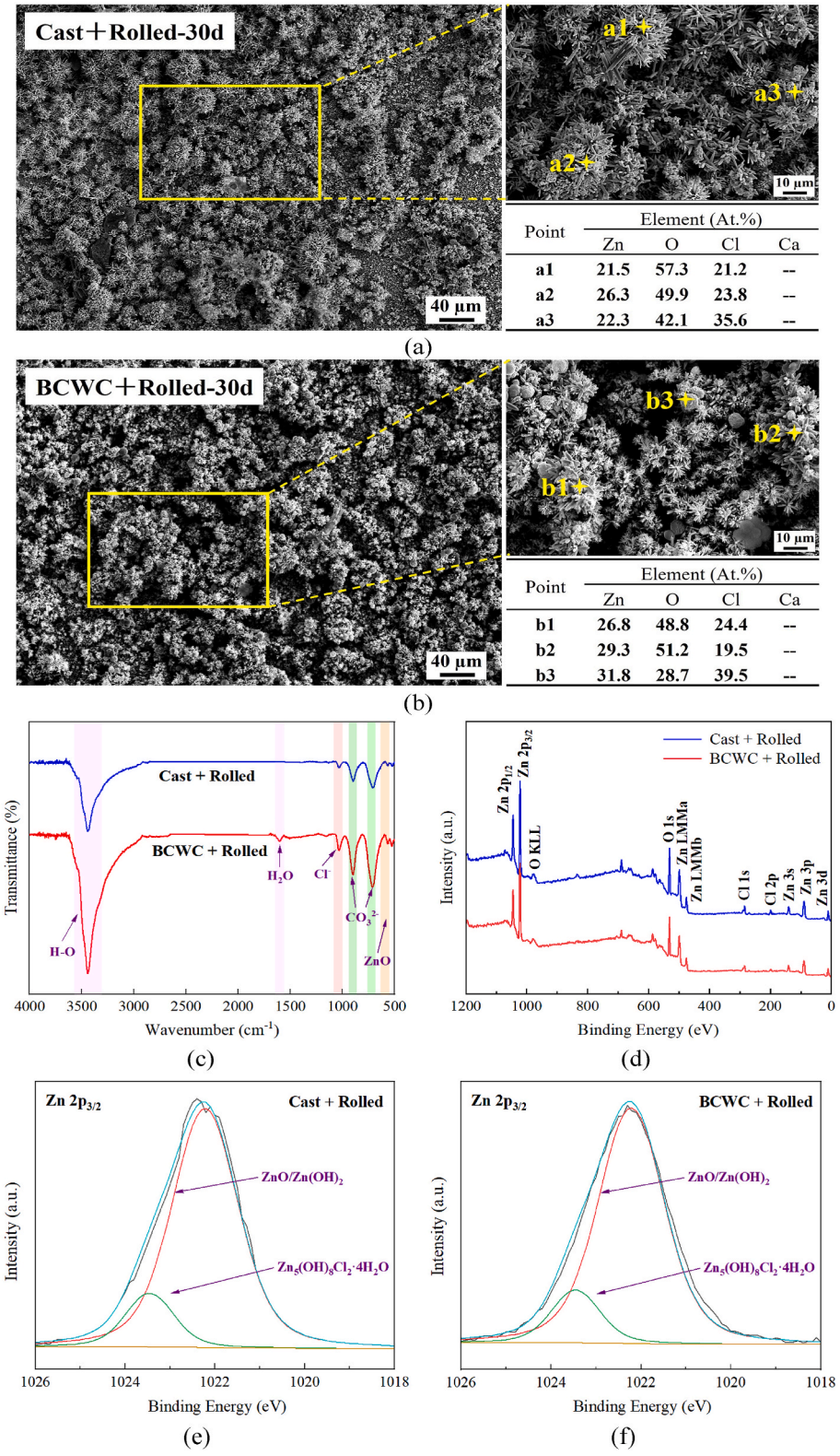

Point	Element (At.%)			
	Zn	O	Cl	Ca
a1	21.5	57.3	21.2	--
a2	26.3	49.9	23.8	--
a3	22.3	42.1	35.6	--

Point	Element (At.%)			
	Zn	O	Cl	Ca
b1	26.8	48.8	24.4	--
b2	29.3	51.2	19.5	--
b3	31.8	28.7	39.5	--

Fig. 8. Immersion in 0.9 % NaCl solution for 30 days: Morphologies of corrosion products on Zn-0.3Ca (CR) in (a) and on Zn-0.3Ca (BR) in (b); (c) FTIR spectra; (d) XPS spectra; (e) XPS spectra of Zn $2p_{3/2}$ at Zn-0.3Ca (CR); (f) XPS spectra of Zn $2p_{3/2}$ at Zn-0.3Ca (BR).

3.5. Cell viability enhanced by BCWC

Fig. 12a shows viability of MC3T3-E1 cells after incubation in 25%–100 % extracts of Zn-0.3Ca (CR) and Zn-0.3Ca (BR) for one day. The higher the extract concentration, the lower the cell viability. The cell viability values are lower than 75 % in 75%–100 % extracts for both alloys. In the 100 % extract, the cell viability ranges from 27.3 % to 45.5 %, indicating grade 3 cytotoxicity according to the ISO 10993-5 standard. When the extract concentration is diluted to 25%–50 %, the cell viability values rise above 80 %, indicating no or slight cytotoxicity.

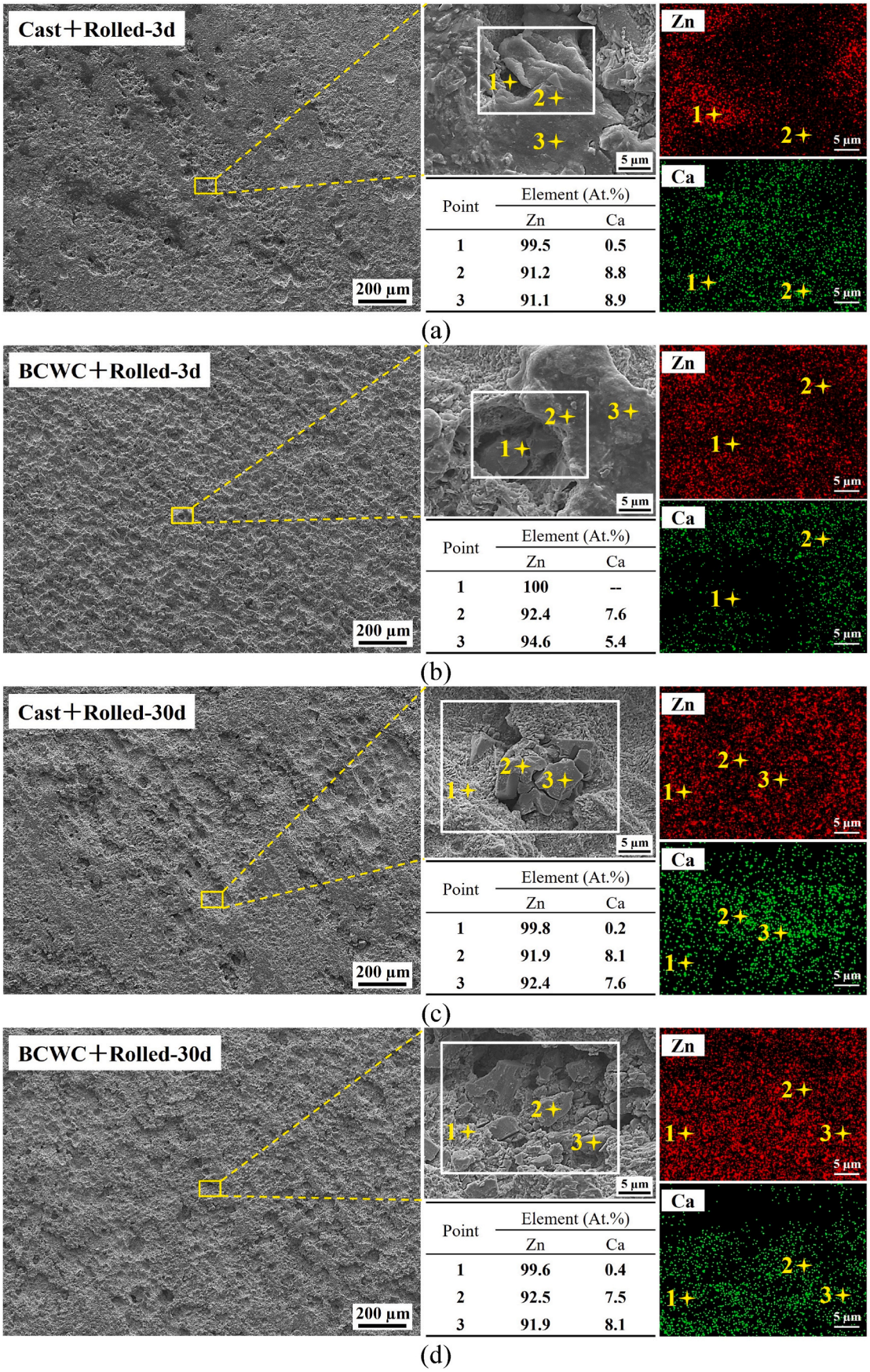

Fig. 9. Surface morphologies after removing corrosion products: (a) Zn-0.3Ca (CR) after 3 days' immersion; (b) Zn-0.3Ca (BR) after 3 days' immersion; (c) Zn-0.3Ca (CR) after 30 days' immersion; (d) Zn-0.3Ca (BR) after 30 days' immersion.

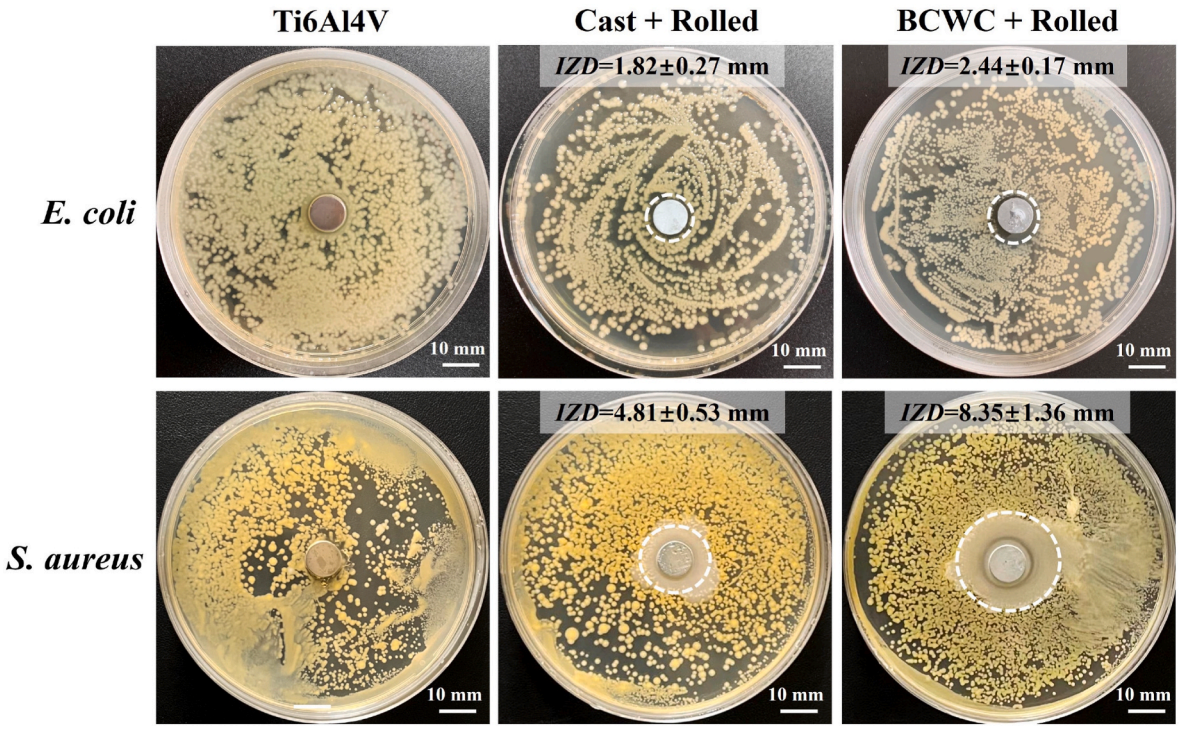

Fig. 10. Antibacterial effects of Zn-Ca alloy samples after co-culturing with *E. coli* and *S. aureus* for 24 h.

Fig. 12b shows viability of MC3T3-E1 cells after 3 days' incubation. In 25%–50 % extracts, cell viability values remain higher than 75 %. In 50 % extracts, the values rise higher than 100 %, promoting cell proliferation. The positive effect becomes more significant in 75 % extracts. After 3 days' cultivation, cell viability value of Zn-0.3Ca (CR) rises from 43.7 % to 91.7 %, while that of Zn-0.3Ca (BR) rises from 64.5 % to 102.2 %. However, in 100 % extracts, cell viability values are still less than 75 %. For Zn-0.3Ca (CR), the cell viability of 3 days is close to that of 1 day in 100 % extracts, remaining below 30 %. By contrast, for Zn-0.3Ca (BR), the cell viability increases significantly from 45.5 % for 1 day to 68.7 % for 3 days in 100 % extracts. The cell viability values of Zn-0.3Ca (BR) are always greater than those of Zn-0.3Ca (CR) at the same condition, so that BCWC enhances biocompatibility.

Fig. 12c shows live/dead staining results of MC3T3-E1 cells that cultivated in 25%–100 % extracts for 3 days, in which the living cells are in green. In 25%–50 % extracts, living cell densities of the two Zn alloys are comparable, which are higher than that of the control group. The cells exhibit a good growth morphology. In 75 % extracts, Zn-0.3Ca (BR) group and the control group exhibit comparable living cell densities, while Zn-0.3Ca (CR) group exhibits a lower density. In 100 % extracts, living cell density of Zn-0.3Ca (CR) is the lowest, and most cells have a spherical morphology, indicating a poor growth state. By contrast, in 100 % extracts of Zn-0.3Ca (BR), although the living cell density is less than that of the control group, a proportion of the cells keep the health fusiform morphology.

Fig. 12d shows cytoskeleton staining results of MC3T3-E1 cells cultivated in 25%–100 % extracts for 3 days. The cytoskeleton is red and the nucleus is blue after staining with rhodamine-phalloidin and DAPI. In 25%–50 % extracts, the cells adhere well on the culture plates. Throughout these cells, cytoskeletons extend and develop lamellipodia and filamentous pseudopods, resulting in high cell densities. This indicates that 25%–50 % extracts of the two Zn alloys can promote cell adhesion, proliferation, and diffusion. In 75 % extracts, living cell density of Zn-0.3Ca (BR) is higher than that of Zn-0.3Ca (CR). Also, cell adhesion morphology of the former alloy is better. In 100 % extract of Zn-0.3Ca (CR), cytoskeletons disappear or shrink sharply to small spheres. By contrast, in 100 % extract of Zn-0.3Ca (BR), cytoskeletons of some cells develop narrow lamellipodia. Thus, Zn-0.3Ca (BR) is more conducive to cell proliferation and diffusion.

3.6. Osteogenic ability enhanced by BCWC

The above cell viability experiments show that in the 25 % and 50 % extracts, the cells exhibit good morphologies and living cell densities. Therefore, 25 % and 50 % extracts of the two Zn alloys are used to further investigate their impacts on the osteogenic differentiation ability of MC3T3-E1 cells.

Alkaline phosphatase (ALP) is an early marker of osteoblast differentiation. Fig. 13a shows ALP staining results of MC3T3-E1 cells cultivated in 25 % extracts for 7 and 14 days. The deeper the purple, the stronger expression of ALP. After 7 days' cultivation, ALP expression levels of Zn-0.3Ca (CR) and Zn-0.3Ca (BR) are higher than that of the control group, among which Zn-0.3Ca (BR) is the highest. The trend of ALP expression levels after 14 days' cultivation is similar to that of 7 days (Fig. 13a). Quantitative analysis of ALP activity is shown in Fig. 13b. Whether it is cultivated 7 days or 14 days, ALP activities are ranked as follows: Zn-0.3Ca (BR) > Zn-0.3Ca (CR) > the control group, indicating that the 25 % extracts of the two Zn alloys promote osteogenic differentiation of the cells.

Fig. 13c shows ALP staining results of MC3T3-E1 cells cultivated in 50 % extracts for 7 and 14 days. The ALP expression of Zn-0.3Ca (CR) is lower than that of the control group, whilst the expression of Zn-0.3Ca (BR) is higher than that of the control group. Fig. 13d shows that the ALP activities are ranked as follows: Zn-0.3Ca (BR) > the control group > Zn-0.3Ca (CR). Thus, the 50 % extract of Zn-0.3Ca (CR) has an inhibitory effect on osteogenic differentiation of MC3T3-E1 cells, while the 50 % extract of Zn-0.3Ca (BR) promotes their osteogenic differentiation. A comparison between Figs. 13b and d shows that the ALP expression levels decrease with the increase of extract concentration. It is clear that the 25 % extracts are more favorable for MC3T3-E1 cell proliferation and osteogenic differentiation. Zn-0.3Ca (BR) shows good osteogenic differentiation ability in both 25 % and 50 % extracts.

Mineralized nodule is a sign of osteoblast differentiation and maturation. Fig. 13e shows the mineralized nodule staining results of MC3T3-

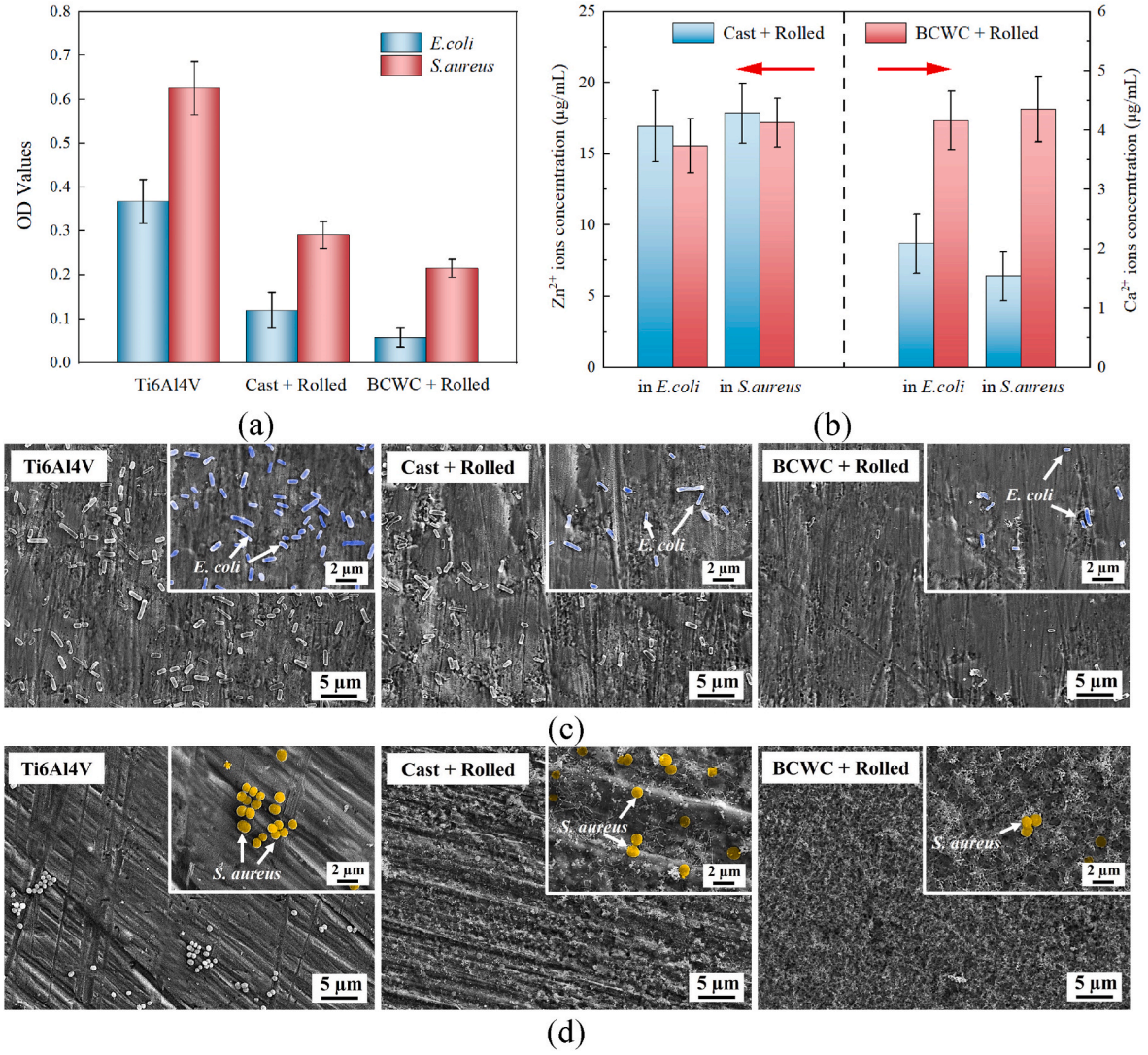

Fig. 11. *E. coli and S. aureus* co-cultured with the Zn-Ca alloys for 24 h: (a) *OD* values in the bacterial fluid; (b) Concentrations of Zn^{2+} and Ca^{2+} in the bacterial fluid; (c) Adhesion morphologies of *E. coli* on alloy surfaces; (d) Adhesion morphologies of *S. aureus* on alloy surfaces.

E1 cells that cultivated in 25 % and 50 % extracts for 14 days. The mineralized nodules are orange-red after staining. Compared to the control group, the cells in the 25 % extracts of Zn-0.3Ca (CR) and Zn-0.3Ca (BR) alloys exhibit a darker orange-red color, indicating a higher presence of mineralized nodules in the osteoblasts. Fig. 13f shows that the mineralization nodule levels in 25 % extracts are ranked as follows: Zn-0.3Ca (BR) > Zn-0.3Ca (CR) > the control group, indicating that this extract concentration can enhance cell matrix mineralization and stimulate osteogenic cell differentiation.

With the increase of extract concentration, the level of mineralized nodules of osteoblasts decreases. In 50 % extracts, mineralization nodule levels are ranked as follows (Fig. 13f): Zn-0.3Ca (BR) > the control group > Zn-0.3Ca (CR). Therefore, the 50 % extracts of Zn-0.3Ca (CR) show some inhibitory effect on mineralization of the cell matrix. However, the 50 % extracts of Zn-0.3Ca (BR) still significantly promote the mineralization, which can increase bone metabolism activity. Therefore, Zn-0.3Ca (BR) is more beneficial for GBR membrane application.

4. Discussion

4.1. The law of metal ion release

Micro-galvanic corrosion between Zn phase and second phase is one of the key factors affecting corrosion uniformity and corrosion rate of Zn alloys [34,52–54]. As shown in Fig. 14a and b, the relative potential of $CaZn_{13}$ phase is approximately 45 mV, which is higher than that of Zn phase. This potential difference will result in faster charge transfer near $CaZn_{13}$/Zn boundaries, thus accelerating degradation of Zn phase. The micro-galvanic corrosion behavior is primarily influenced by features of $CaZn_{13}$ particles, including volume fraction, specific surface area, and distribution.

According to a previous study [33], the calculation formula for the equilibrium volume fraction of $CaZn_{13}$ in Zn-Ca alloy (i.e., V_{CaZn13}) is as follows:

$$W_{CaZn13} = W_{Ca}/4.5, \tag{2}$$

$$V_{CaZn13} = (W_{CaZn13} / \rho_{CaZn13}) / [W_{CaZn13} / \rho_{CaZn13} + (100 - W_{CaZn13}) / \rho_{Zn}], \tag{3}$$

where W_{Ca} is Ca addition in wt.%, ρ_{CaZn13} is the density of $CaZn_{13}$ (6.62 g/cm^3 [33]), and ρ_{Zn} is the density of Zn (7.14 g/cm^3 [69]).

W_{Ca} values of Zn-0.3Ca (CR) and Zn-0.3Ca (BR) alloys are 0.34 wt% and 0.36 wt%, respectively. Thus, it can be calculated that V_{CaZn13} value of Zn-0.3Ca (CR) is 8.1 vol%, and that of Zn-0.3Ca (BR) is 8.6 vol%. It can be seen from Fig. 4f that for both the alloys, the differences between the calculated and the measured volume fractions are below 5 %,

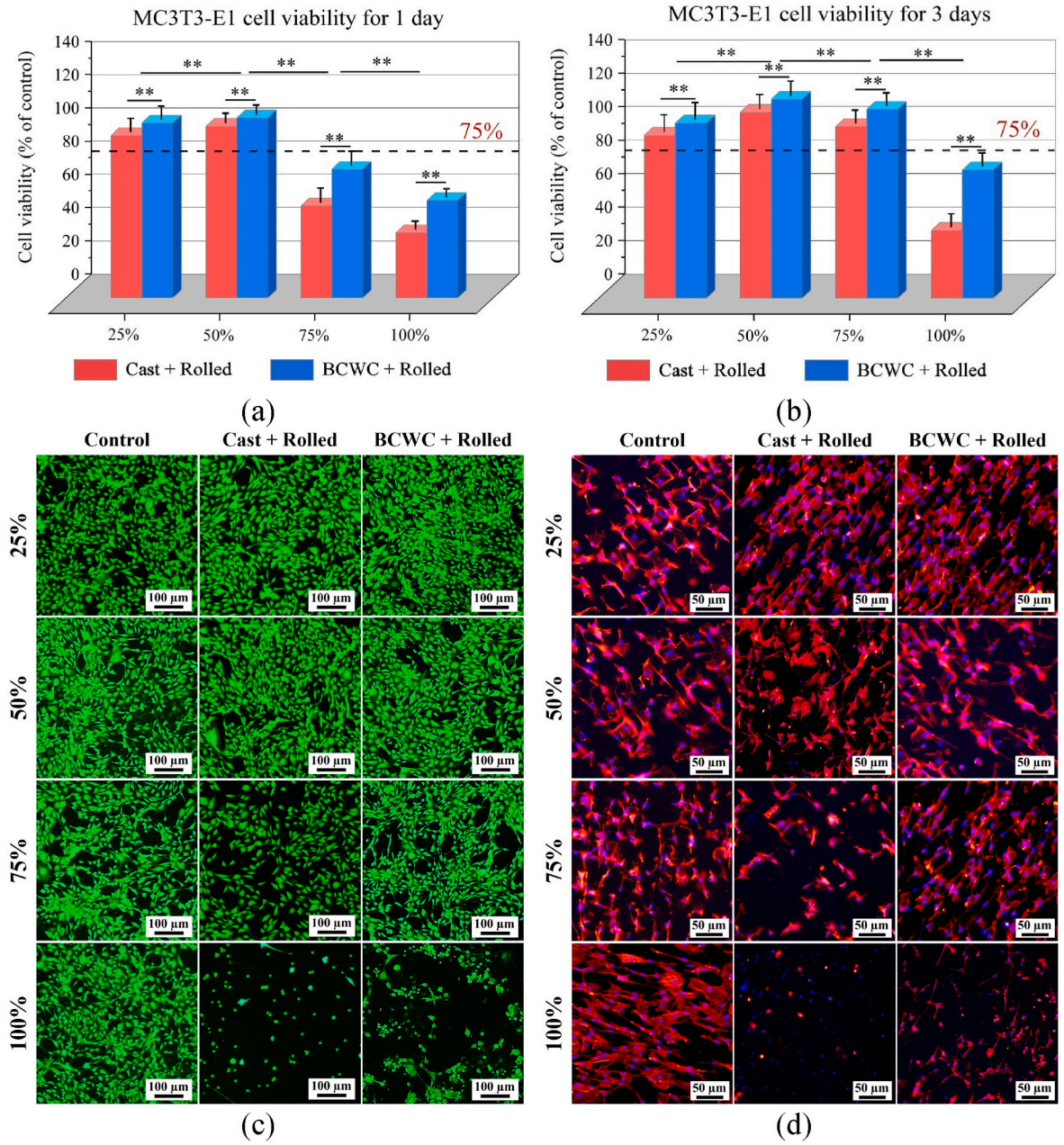

Fig. 12. MC3T3-E1 cells cultured in extracts of the Zn alloys: Cell viability values after 1 day cultivation in (a) and after 3 days' cultivation in (b); (c) AM/PI live/dead staining images of the cells after 3 days' cultivation; (d) CLSM images of the cell cytoskeleton (red) and nucleus (blue) stained by rhodamine-phalloidin and DAPI.

suggesting that only a small amount of Ca is dissolved into the Zn matrix. Since these V_{CaZn13} values are close, the influence of V_{CaZn13} on the difference of corrosion behaviors of the two alloys should be negligible.

The numbers $CaZn_{13}$ particles in Zn-0.3Ca (CR) and Zn-0.3Ca (BR) are represent as n_1 and n_2, respectively. Then, it can be calculated that:

$$n_2 / n_1 = \left(V_2 \cdot r_1^3\right) / \left(V_1 \cdot r_2^3\right), \tag{4}$$

where V refers to volume fraction of $CaZn_{13}$ particles, r refers to the average size (in equivalent diameter) of $CaZn_{13}$ particles, and the subscripts '1' and '2' refer to Zn-0.3Ca (CR) and Zn-0.3Ca (BR), respectively. It can be seen from Fig. 4f that r_1 is 10.8 μm, and r_2 is 2.1 μm. V_1 is 8.1 vol %, and V_2 is 8.6 vol%. Then, it can be calculated that $n_2 = 144n_1$, which means that micro-galvanic corrosion sites in Zn-0.3Ca (BR) are 144 times of those in Zn-0.3Ca (CR).

Due to the influence of galvanic corrosion, the Zn phase around the $CaZn_{13}$ particles is preferentially corroded, resulting in the formation of corrosion gap at the interface between the $CaZn_{13}$ particles and the Zn phase (as shown in Fig. 10a and b). According to the law of crevice corrosion [70,71], as the immersion time increases, the Cl^- ions in the 0.9 % NaCl solution tends to continuously accumulate in the crevice. Which promotes the dissolution of $CaZn_{13}$ particles and Zn phase near the two-phase interface (as shown in Fig. 10c and d). The dissolution of $CaZn_{13}$ particles releases Ca^{2+} ions into the solution. The released number (N) of Ca^{2+} ions can be expressed by the following formula:

$$N = J \cdot SSA \cdot \left(4 / 3 \cdot \pi r^3\right) \cdot n \cdot t, \tag{5}$$

where J refers to flux of Ca^{2+} ions from a $CaZn_{13}$ particle (unit: number·μm^{-2}·s^{-1}), SSA refers specific surface area of a $CaZn_{13}$ particle (unit: μm^{-1}), r refers to diameter of a $CaZn_{13}$ particle (unit: μm), n refers to number of a $CaZn_{13}$ particle (unit: number), t refers to immersion time

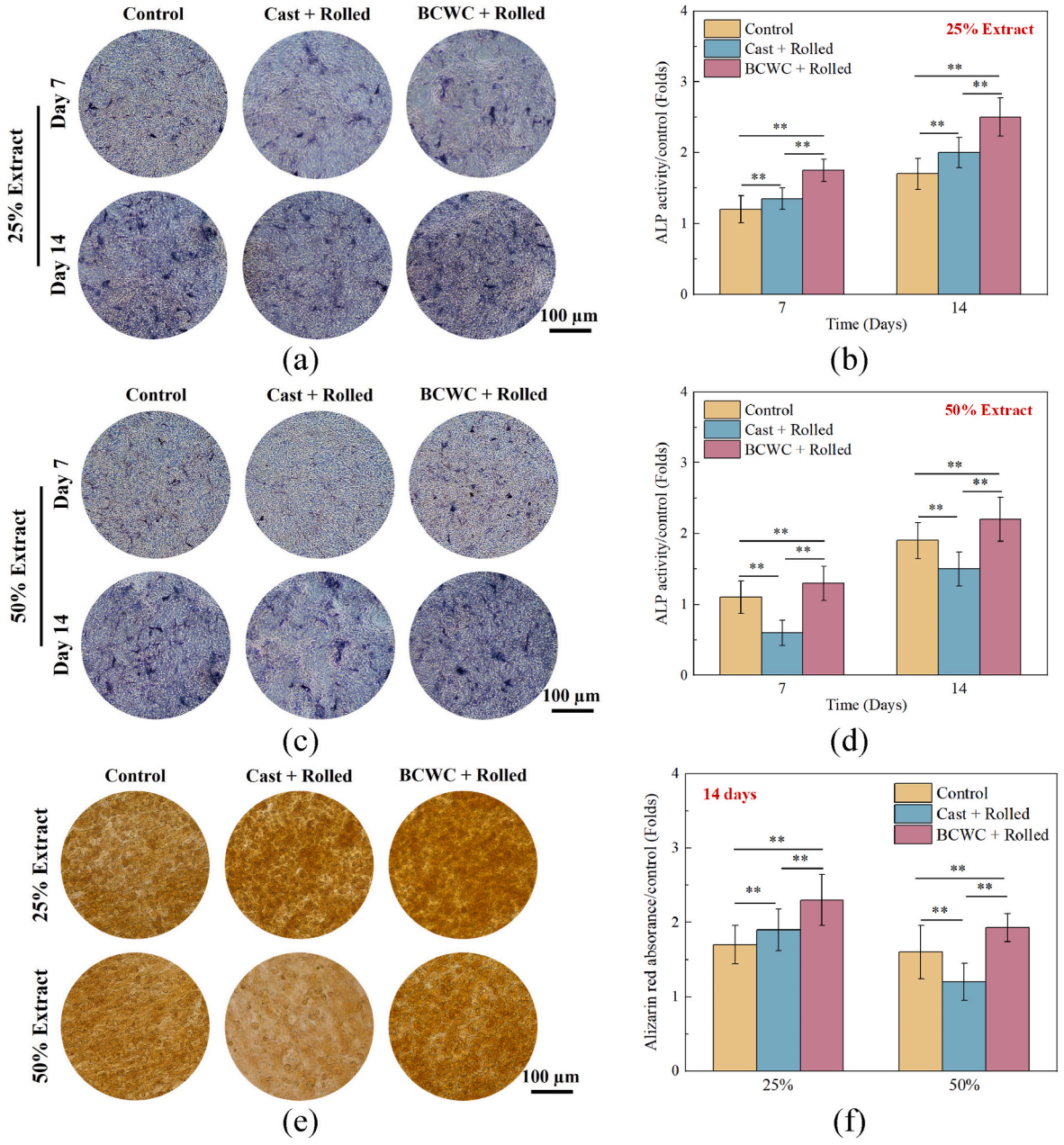

Fig. 13. Expression of osteogenic activity *in vitro*: (a) ALP expression in 25 % extracts; (b) ALP activity in 25 % extracts; (c) ALP expression in 50 % extracts; (d) ALP activity in 50 % extracts; (e) ARS staining at day 14; (f) Quantitative analysis of ARS staining at day 14.

(unit: s).

The immersion times of the two alloys are the same, i.e., t in Eq. (5) is the same. Subscripts '1' and '2' also be used to refer to Zn-0.3Ca (CR) and Zn-0.3Ca (BR), respectively. It can be calculated that $SSA_2 = 5.1SSA_1$. J is mainly affected by the potential difference between $CaZn_{13}$ and Zn, corrosion medium, corrosion products and other factors. Initially, J values of the two alloys are the same. Therefore:

$$N_2/N_1 = (SSA_2 \cdot r_2^3 \cdot n_2)/\ (SSA_1 \cdot r_1^3 \cdot n_1), \tag{6}$$

From Eq. (4), it can be further obtained that:

$$N_2/N_1 = (SSA_2 \cdot V_2)/\ (SSA_1 \cdot V_1). \tag{7}$$

Since $V_2/V_1 = 8.6$ vol%/8.1 vol% ≈ 1 (accurately 1.06), it can be calculated that $N_2/N_1 \approx SSA_2/SSA_1 = 5.1$. This means that theoretically the number of Ca^{2+} ions released by Zn-0.3Ca (BR) is 5.1 times that of Zn-0.3Ca (CR) in the early stage of immersion. Correspondingly, a ratio (r_{Ca}) of measured Ca^{2+} ions is defined:

$$r_{Ca} = C_{2c}/C_{1c}, \tag{8}$$

where C_{2c} refers to the measured amount of Ca^{2+} ions released from Zn-0.3Ca (BR) at a certain time, and C_{1c} refers to that released from Zn-0.3Ca (CR) at the same time. According to the data in Fig. 15a, r_{Ca} values of different days are calculated as shown in Fig. 15b. At day 1, r_{Ca} is equal to 5.03, which is close to its theoretical of 5.1 (Fig. 15b). This indicates that the release of Ca^{2+} ions in Zn-Ca alloy are determined by the average specific surface area of $CaZn_{13}$ particles at the initial stage of immersion. This proposes an important direction for microstructure control of Zn-Ca alloys, i.e., adjusting the release of Ca^{2+} ions through controlling $CaZn_{13}$ particle size.

With the increase of immersion time, r_{Ca} value decreases in a parabolic manner (Fig. 15b). After fitting, r_{Ca} varies with immersion time (t) as follows:

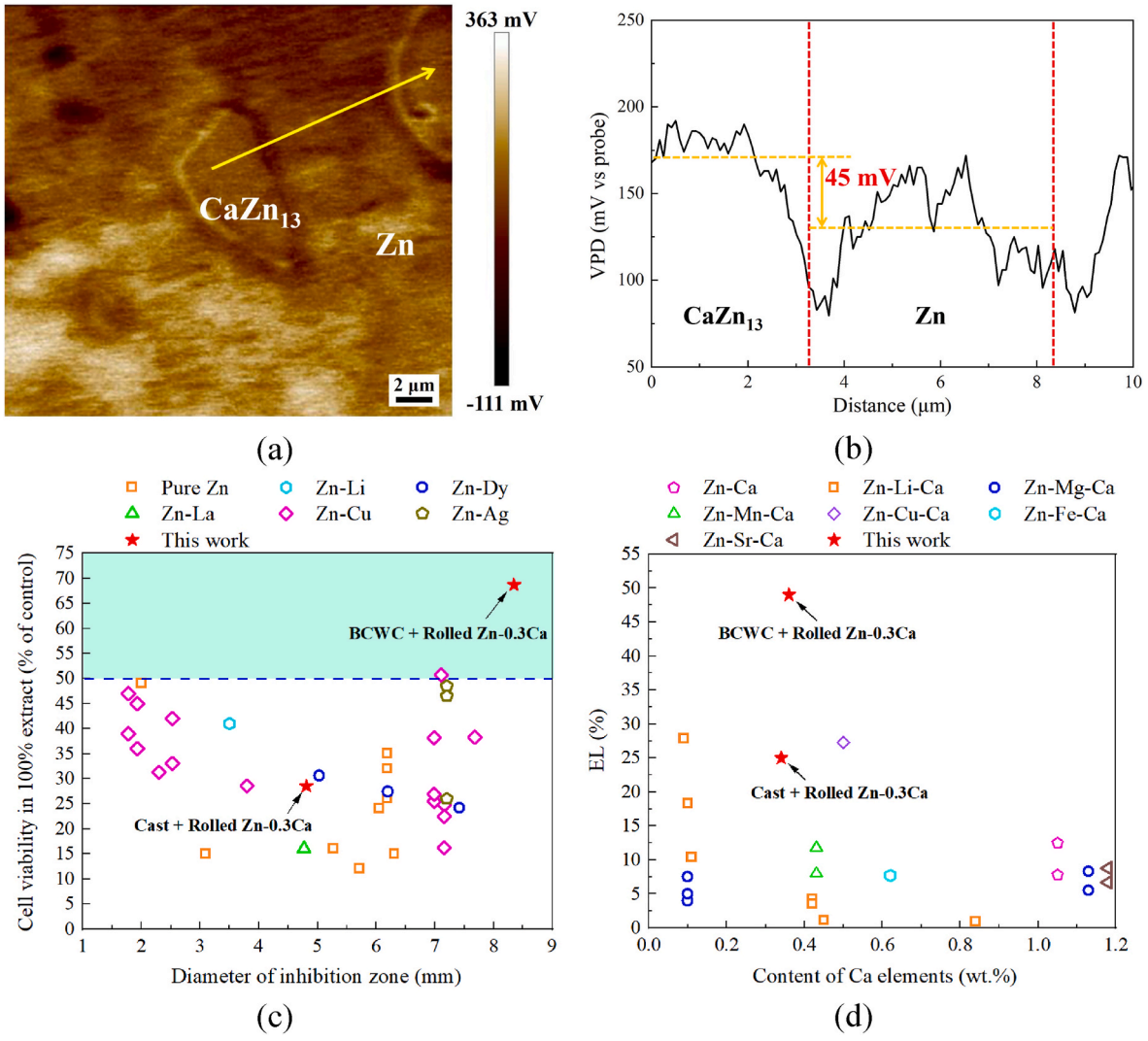

Fig. 14. (a) SKPFM of $CaZn_{13}$ and Zn; (b) The Volta potential difference (VPD) distribution along the yellow arrowed line in (a); (c) MC3T3-E1 cell viability in 100 % extract and *S. aureus IZDs* of Zn alloys. Data are collected from literatures [36,55–63]; (d) ELs and Ca content of wrought Zn-Ca-based alloys. Data are collected from literatures [27–29,32–34,64–68].

$$r_{Ca} = 5.1 + 3.6\left(t^{-1/2} - 1\right), \tag{9}$$

After immersion for 20 days, the r_{Ca} value tended to be stable, $r_{Ca} \approx 2$. This is because the corrosion products cover the alloy surface and hinder the release of Ca^{2+}.

Different from the trend of Ca^{2+} ions, Zn^{2+} ions show a linear relation with immersion days (Fig. 15c). Analogously to r_{Ca} in Eq. (7), the ratio of measured Zn^{2+} ions (r_{Zn}) can be defined. Fig. 15d shows that r_{Zn} values increase fast to a stable level around 1. After immersion for 14 days, r_{Zn} values keep at 1.06 (Fig. 15d), which is close to the value of $(1-V_2)/(1-V_1)$, i.e., 0.99. This indicates that the release of Zn^{2+} is determined by the volume fraction of Zn phase.

4.2. Corrosion reactions of Zn-Ca alloy

Some extensive studies have reported in *vitro* corrosion behaviors of Zn alloys containing Ca [27,30,34]. Commonly used corrosion media include 0.9 % NaCl solution, Hank's Balanced Salt Solution (HBSS), and simulated body fluid (SBF). The alloys undergo anodic and cathodic reactions in these media [34]. Reactions are shown as follows:

$$\text{Anodic reaction: } Zn \rightarrow Zn^{2+} + 2e^{-}, \tag{10}$$

$$\text{Cathodic reaction: } O_2 + 2H_2O + 4e^{-} \rightarrow 4OH^{-}, \tag{11}$$

$$Zn^{2+} + 2OH^{-} \rightarrow Zn(OH)_2, \tag{12}$$

$$Zn(OH)_2 \rightarrow ZnO + H_2O, \tag{13}$$

$$Zn(OH)_2 + Cl^{-} \rightarrow Zn^{2+} + 2OH^{-} + 2Cl^{-}. \tag{14}$$

The reaction of pure Zn with water produces OH−, which combines with Zn^{2+} to form $Zn(OH)_2$. $Zn(OH)_2$ further reacts to produce the more stable ZnO. The Cl^- ions in the solution destroy the generated $Zn(OH)_2$, causing it to dissolve and release Zn^{2+} ions, thereby promoting corrosion of Zn alloys. In the initial stage of immersion, the primary corrosion products are mainly ZnO and $Zn(OH)_2$ [50]. The types of ions in different corrosive media are different, and they will produce different corrosion products with the extension of immersion time.

In 0.9 % NaCl solution, Cl^- ions migrate to the anode position under the influence of electric field and react with Zn^{2+}, OH^-, and $Zn(OH)_2$. The reaction equations are as follows:

$$5Zn^{2+} + 8OH^{-} + 2Cl^{-} + H_2O \rightarrow Zn_5(OH)_8Cl_2{\cdot}H_2O, \tag{15}$$

$$5Zn(OH)_2 + 2Cl^{-} + H_2O \rightarrow Zn_5(OH)_8Cl_2{\cdot}H_2O + 2OH^{-}. \tag{16}$$

The corrosion product is $Zn_5(OH)_8Cl_2{\cdot}H_2O$, and the corrosion morphology is rod-like or needle-like, as shown in Fig. 8a and b.

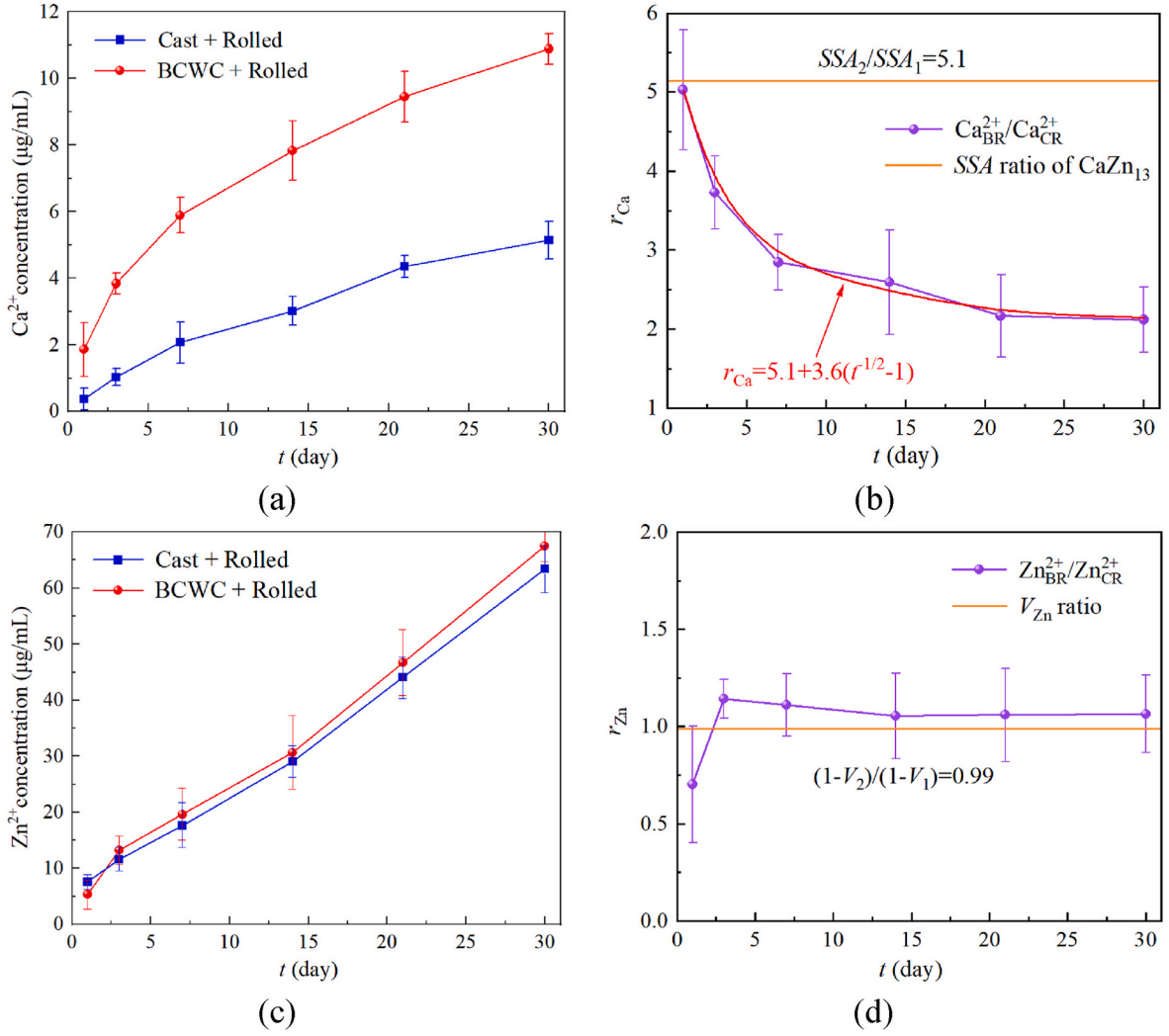

Fig. 15. Immersion in 0.9 % NaCl solution for 30 days: (a) Cumulative release of Ca^{2+}; (b) r_{Ca} values in function of time; (c) Cumulative release of Zn^{2+}; (d) r_{Zn} values in function of time. In the figures, '*t*' refers to immersion time.

Beside Cl^- ions, SBF and HBSS also contain HPO_4^{2-}, HCO_3^-, Ca^{2+}, and Mg^{2+} ions [46,51]. The composition of these inorganic salts are more closely resembles that of human body fluids [51]. Previous studies [30] have shown that the corrosion products of Zn-Ca alloys in HBSS primarily consist of C, O, P, Ca, and Zn elements, with the main components being phosphates and carbonates. The corrosion products are spherical [30,50]. The reactions are as follows:

$$3Zn^{2+} + 2HPO_4^{2-} + 2OH^- + 2H_2O \rightarrow Zn_3(PO_4)_2{\cdot}4H_2O, \quad (17)$$

$$3Ca^{2+} + 2PO_4^{3-} \rightarrow Ca_3(PO_4)_2, \quad (18)$$

$$2M^{2+} + 2HCO_3^- + 2OH^- \rightarrow ZMCO_3 + 2H_2O,\ M = Zn \text{ or } Mg, \quad (19)$$

$$5Zn^{2+} + 2HCO_3^- + 8OH^- \rightarrow Zn_5(CO_3)_2(OH)_6 + 2H_2O, \quad (20)$$

$$Zn_5(CO_3)_2(OH)_6 + 4OH^- \rightarrow 5\ ZnO + 2CO_3^{2-} + 5H_2O, \quad (21)$$

$$Ca^{2+} + CO_3^{2-} \rightarrow CaCO_3. \quad (22)$$

The presence of HPO_4^{2-} and HCO_3^- in SBF or HBSS results in the deposition of $Ca_3(PO_4)_2$ and $CaCO_3$, which can hinder the erosion of Cl^- to a certain extent, thus slowing down the corrosion of Zn alloys [72,73]. This explains why the corrosion rate of Zn alloys in 0.9 % NaCl solution is often higher than those in HBSS and SBF.

4.3. How to break the tradeoff between antibacterial ability and biocompatibility?

Fig. 14c collects *IZD* values of 35 kinds of Zn alloys against *S. aureus* and their viability values of MC3T3-E1 cells in 100 % extract *in vitro*. It can be seen that all the Zn alloys have *IZD* values > 1 mm, indicating strong antibacterial activity due to the broad-spectrum antibacterial ability of Zn^{2+} ions [18,21,74]. Zn^{2+} ions can induce production of reactive oxygen species (ROS), destroy structures of bacteria, affect internal metabolism and DNA replication of bacteria, hinder growth and proliferation of bacteria [7,75]. Positively charged Zn^{2+} ions can adsorb onto bacterial cell membrane and disrupt its integrity, leading to bacterial inactivation [76]. In general, the antibacterial ability in Zn alloys is proportional to concentration of released Zn^{2+} ions [77]. In a previous study, when concentration of Zn^{2+} ions was about 12.2 μg/mL, the antibacterial rate against *S. aureus* was approximately 80.6 % [78]. In this study, the amounts of Zn^{2+} ions released by the two alloys in *S. aureus* fluids are 17.8 μg/mL and 17.2 μg/mL respectively (Table 4), which are much higher than 12.2 μg/mL. As a result, the two Zn-Ca alloys exhibit a strong antibacterial effect.

In *S. aureus* fluids, the Zn^{2+} ions released from Zn-0.3Ca (BR) (17.2 μg/mL) is lower than that from Zn-0.3Ca (CR) (17.8 μg/mL) (Table 4). However, the *IZD* value of Zn-0.3Ca (BR) against *S. aureus* is about 74 % larger than that of Zn-0.3Ca (CR) (Fig. 10). This is because Ca^{2+} ions are

also positively charged and can react with bacterial biofilms. This interaction interferes with the permeability of biofilms and induces bacterial rupture [79]. Zhao et al. [80] reported that the amount of Ca^{2+} ions released from TiN(Ca) coating on TI6Al4V was only 0.06–0.10 μg/mL, but the antibacterial rate reached 49.8 %. In this study, the Ca^{2+} ions released from Zn-0.3Ca (BR) in *S. aureus* fluid is 4.4 μg/mL (Table 4), which is about 2.9 times of that from Zn-0.3Ca (CR). The total amount of released Zn^{2+} and Ca^{2+} ions from Zn-0.3Ca (BR) is 21.6 μg/mL, which is about 12 % higher than that from Zn-0.3Ca (CR) (Table 4). Due to the synergistic antibacterial effect of Zn^{2+} and Ca^{2+} ions, Zn-0.3Ca (BR) exhibits an improved antibacterial ability.

Similarly, the released amount of Zn^{2+} ions from Zn-0.3Ca (BR) in *E. coli* fluid is 15.6 μg/mL, which is lower than 16.9 μg/mL of Zn-0.3Ca (CR). However, the *E. coli IZD* value of Zn-0.3Ca (BR) is about 34 % larger than that of Zn-0.3Ca (CR) (Fig. 10). The reason is that the total amount of Zn^{2+} and Ca^{2+} ions released from Zn-0.3Ca (BR) in *E. coli* fluid is about 4 % higher than that of Zn-0.3Ca (CR) (Table 4). The improvement of antibacterial ability against *E. coli* is not as high as that against *S. aureus*, since the increase of the total released amount of the metal ions is reduced.

As shown in Fig. 14c, although all of the Zn alloys have good antibacterial abilities, the viability values of MC3T3-E1 cells in 100 % extracts of most Zn alloys are less than 50 %. This is because MC3T3-E1 cells have Zn^{2+} concentration dependence [22]. When the Zn^{2+} concentration exceeds 12.2 μg/mL, it surpasses the optimal growth threshold of MC3T3-E1 cells (12.1 μg/mL), resulting in decreased cell viability [24]. The release amount of Zn^{2+} in 100 % extract of Zn-0.3Ca (CR) is 20.4 μg/mL, which is much higher than the threshold. So, the MC3T3-E1 cell viability is only 28 % in 100 % extract of Zn-0.3Ca (CR) (Fig. 12b). Diluted extracts are commonly used to assess cytotoxicity of biodegradable metals [81]. When the extract of Zn-0.3Ca (CR) is diluted to 75 %, no cytotoxicity is detected in the condition of 15.3 μg/mL Zn^{2+} and 1.51 μg/mL Ca^{2+}. This indicates that Ca^{2+} ions can improve the tolerance of MC3T3-E1 cells to Zn^{2+}, i.e., elevating the optimal growth threshold.

Consistently, it's worth noting that the amount of Zn^{2+} released from Zn-0.3Ca (BR) in 100 % extract is 17.6 μg/mL, but the cells still show good spreading morphology and the highest cell viability of 68.7 % in Fig. 14c. The total released amount of Zn^{2+} and Ca^{2+} ions in 100 % extract of Zn-0.3Ca (BR) is close to that of Zn-0.3Ca (CR) (Table 4). However, the released Ca^{2+} amount from Zn-0.3Ca (BR) accounts for 23 % of the total released amount of Zn^{2+} and Ca^{2+}, which is 2.3 times of that from Zn-0.3Ca (CR). Ca^{2+} ions are necessary for cell proliferation [82]. Ca^{2+} ions can stimulate activation of integrin-mediated signaling pathways, which promote cell adhesion, proliferation, and differentiation [83,84]. It reveals that toxicity of 100 % extract can be alleviated through elevating proportion of released Ca^{2+} ions.

The antibacterial activity in this study is the result of transition from single Zn^{2+} ions to multi-ions synergy. When the total released amounts of Zn^{2+} and Ca^{2+} ions are greater than 15 μg/mL, antibacterial effect can be enhanced. Under the premise of keeping the total released amount of Zn^{2+} and Ca^{2+} ions unchanged, increasing the ratio of Ca^{2+} ions can reduce cytotoxicity and thus break the trade-off between antibacterial ability and biocompatibility.

Table 4
Released ion concentrations in bacteria and cell culture medium.

Alloy	Test type	Ion concentration (μg/mL)			$Ca^{2+}/(Zn^{2+}+Ca^{2+})$
		Zn^{2+}	Ca^{2+}	$Zn^{2+}+Ca^{2+}$	
Cast + Rolled	in *E. coli*	16.9 ± 2.5	2.1 ± 0.6	19.0	11 %
	in *S. aureus*	17.8 ± 2.1	1.5 ± 0.4	19.3	8 %
	in cell media	20.4 ± 1.4	2.3 ± 0.7	22.7	10 %
BCWC + Rolled	in *E. coli*	15.6 ± 1.9	4.1 ± 0.5	19.7	21 %
	in *S. aureus*	17.2 ± 1.7	4.4 ± 0.6	21.6	20 %
	in cell media	17.6 ± 2.3	5.2 ± 0.3	22.8	23 %

4.4. The mechanism of increasing plasticity by BCWC

EL of Zn alloys in function of Ca addition is shown in Fig. 14d. Overall, the EL decreases with the increase of Ca content. The majority of the reported Zn-Ca alloys exhibit ELs less than 20 %. However, Zn-0.3Ca (BR) exhibits an EL as high as 49 %, which is the highest among Ca-containing Zn alloys.

4.4.1. Effect of $CaZn_{13}$ particle refinement on plasticity

$CaZn_{13}$ is a major second phase of Ca-containing Zn alloys. $CaZn_{13}$ particles are easy to coarsen along <111> and <010> directions during alloy melt solidification [33]. Coarse $CaZn_{13}$ particles are difficult to be completely broken up into small particles through plastic deformation processing. Cracks in $CaZn_{13}$ particles serve as preset micro cracking sources of the samples during tensile testing, leading to early fracture [33]. Huang et al. [64] reported that Zn-0.6Mg-0.1Ca alloy prepared by equal channel angular pressing (ECAP) has a limited EL of less than 10 %. Phase size mismatch ratio (r_{psm}) reaches 15 in this alloy, which is defined by the ratio of $CaZn_{13}$ particle size (d_{SP}) to Zn grain size (d_Z), i.e., $r_{psm} = d_{SP}/d_Z$. Such a significant difference of size between the hard $CaZn_{13}$ particles and the soft Zn matrix leads to strain incompatibility during deformation, resulting in a high concentration of local stress in vicinity of phase boundaries, damaging the alloy's plasticity [64,85].

For Zn-0.3Ca (BR) alloy, the size of Zn grains is refined to 1.4 ± 0.8 μm, and the size of $CaZn_{13}$ particles is refined to 2.1 ± 1.1 μm (Fig. 4e and f). The ratio r_{psm} is reduced to about 1.7, so that Zn grains and $CaZn_{13}$ particles can cooperate with each other more easily through grain boundary slipping during plastic deformation. Similar phenomenon can be found in Zn-1Cu-0.5Ca alloy with r_{psm} about 1.5 [34]. Therefore, we propose an idea of improving plasticity of Ca-containing Zn alloys as follows: Refine the size of $CaZn_{13}$ particles to be close to that of its surrounding Zn grains, and both are controlled to be less than 5 μm.

4.4.2. Effect of grain refinement on plasticity

Grain refinement at micron scale often results in simultaneous increase in strength and ductility of metallic materials [86]. Sizes of Zn grains and $CaZn_{13}$ particles in Zn-0.3Ca (BR) are refined by approximately 55 % and 81 % compared to those in Zn-0.3Ca (CR), respectively (Fig. 4e and f). However, this grain refinement leads to softening of the alloy. The EL of Zn-0.3Ca (BR) increases to about twice that of Zn-0.3Ca (CR), but its YS decreases by 22 % (Fig. 2b). The refinement of Zn grains causes a transformation in the deformation mechanism from dislocation slip and twinning to grain boundary slip, resulting in the softening effect [40]. Similar phenomena have been observed in other Zn alloys. For instance, Shi et al. [87] discovered that grain size of Zn-0.76Mn alloy was refined to 2 μm, resulting in an EL of 94 %. Bednarczyk et al. [88] found that grain size of Zn-0.5Cu alloy was refined to 1.32 μm, leading to an EL of 375 % at room temperature. When the grain size was further refined to 1 μm, the EL increased to 437 %.

On the other hand, $CaZn_{13}$ particles can promote dynamic recrystallization of their surrounding Zn grains during the tensile testing process through particle-stimulated nucleation (PSN). Similar phenomenon also appears in tensile testing of Zn-0.8Mn alloy, during which $MnZn_{13}$ particles promote recrystallization of Zn grains [89]. As shown in Fig. 6c and f, some small recrystallized grains are distributed around $CaZn_{13}$ particles. According to Eq. (4) in *Section* 4.1, the number of $CaZn_{13}$ particles in Zn-0.3Ca (BR) is 144 times that in Zn-0.3Ca (CR). A higher number of $CaZn_{13}$ particles results in a more pronounced PSN

effect, leading to a greater degree of dynamic recrystallization and lower dislocation density in the alloy. When the softening effect due to dynamic recrystallization surpasses the work hardening effect caused by dislocation accumulation, the strength of the alloy decreases while its plasticity improves. Density distribution maps of geometrically necessary dislocations (GNDs) of the two alloys are shown in Fig. 16a and b. The dislocation density of Zn-0.3Ca (BR) is lower than that of Zn-0.3Ca (CR). Specifically, the average dislocation density (ρ^{GND}) of Zn-0.3Ca (BR) is 1.1 × 10^{14} m^{-2}, which is only one-third of that of Zn-0.3Ca (CR) (Fig. 16e).

4.4.3. *Effect of texture on plasticity*

Texture modification is an effective method to improve the room temperature plasticity and formability of hexagonal close-packed (HCP)

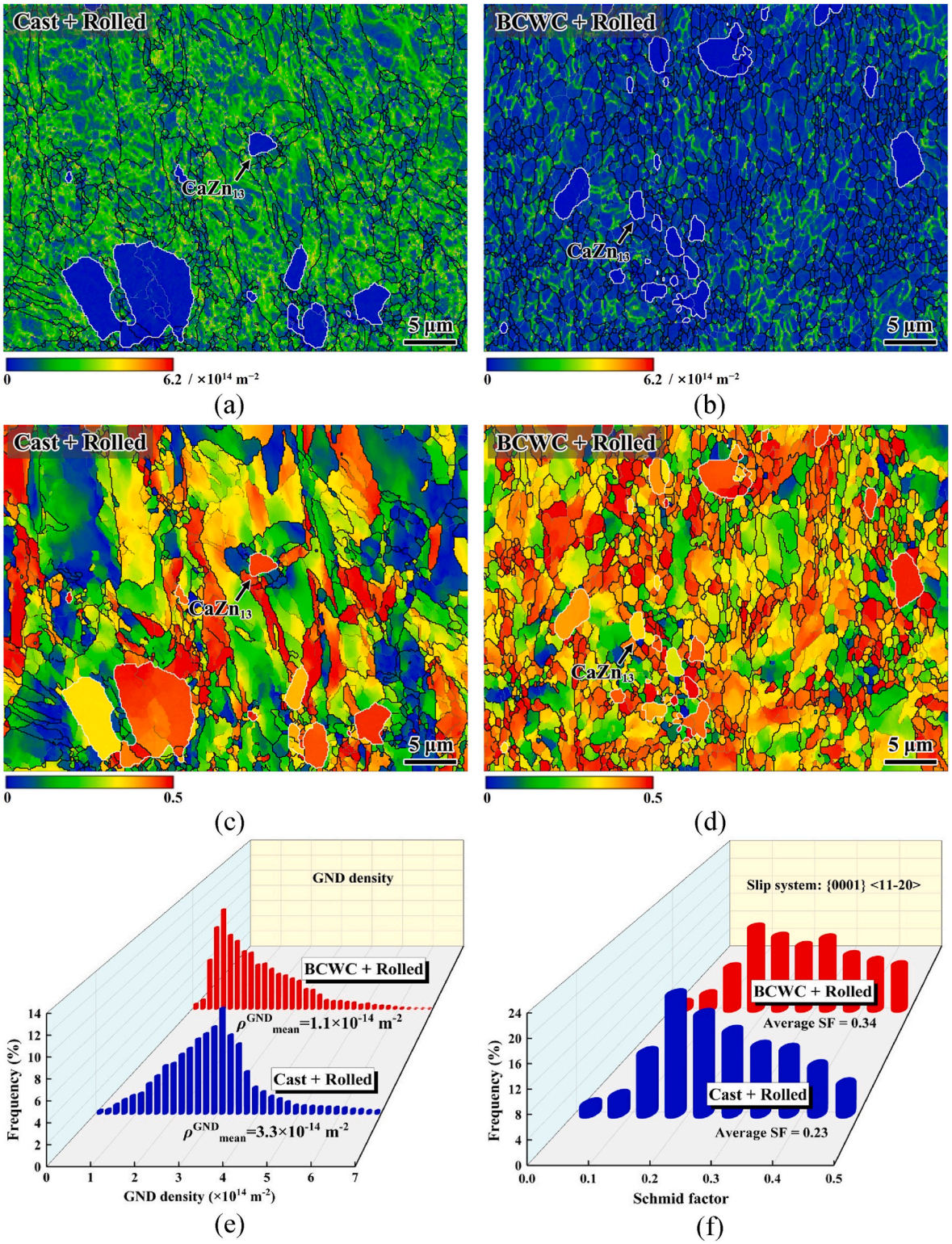

Fig. 16. Geometrically necessary dislocations (GND) density maps of Zn-0.3Ca (CR) in (a) and Zn-0.3Ca (BR) in (b); Schmid factor (SF) maps for the (0001) <11–20> basal slip of Zn-0.3Ca (CR) in (c) and Zn-0.3Ca (BR) in (d); (e) Distributions of the GND density values; (f) Distributions of the SF values.

metals [90]. For Zn-0.3Ca (CR), the pole of (0001) close to ND (Fig. 6g) is due to {0001}<11–20> basal slip, while that of (0001) close to RD (Fig. 6g) is due to {10–12}<10–11> compressive twinning that can rotate a Zn crystal about 86° [39]. For Zn-0.3Ca (BR), two (0001) basal poles tilted about 25° from ND toward RD (Fig. 6h). This split basal texture is typical for HCP metals with $c/a > 1.633$, such as Zn (1.856), due to combination of {0001}<11–20> basal slip and {11–22}<11-2-3> pyramidal slip [91,92].

The change of texture will change Schmit factor (SF) of basal slip system. The SF maps for basal <a> slip (i.e., {0001}<11–20>) of the two alloys are shown in Fig. 16c and d. The ratio of warm colored grains in Zn-0.3Ca (BR) is higher than that in Zn-0.3Ca (CR), indicating that more grains in the former alloy have high SFs of basal slip. The average SF value is 0.34 for Zn-0.3Ca (BR) and is 0.23 for Zn-0.3Ca (CR) (Fig. 16f). Thus, Zn-0.3Ca (BR) is easier to deform, leading to a higher EL and a lower YS. Additionally, ELs of other HCP metals can also be improved through formation of symmetric double-peak textures similar to that of Zn-0.3Ca (BR), such as Mg-Gd, Mg-Ce and Mg-Y alloys [93–95].

Texture weakening is another reason for the improved EL of Zn-0.3Ca (BR) (Fig. 6g and h). Zn-0.3Ca (BR) exhibits a relatively weak (0001) basal texture with the maximum intensity of 5.2 mrd, which is 20 % lower than that of Zn-0.3Ca (CR). The effect of texture on YS can be explained by the following equation [96]:

$$\sigma_t = (0.3/m - 1) \times kd^{-0.5}, \quad (23)$$

where m refers to the average SF of basal slip; d refers to the average size of Zn grains. For calculation, subscripts '1' and '2' refer to Zn-0.3Ca (CR) and Zn-0.3Ca (BR), respectively. As mentioned above, m_1 is 0.23, d_1 is 3.1 μm, m_2 is 0.34, and d_2 is 1.4 μm. Then, it can be calculated that $\sigma_1 =$ 67.6 MPa and $\sigma_2 = -17.2$ MPa. It is clear that the weakened texture leads to the softening of Zn-0.3Ca (BR).

5. Conclusions

In this paper, a BCWC-and-rolling method is proposed for controlling the microstructure of Zn-0.3Ca alloy. Conclusions are as follows.

(1) BCWC-rolling refines $CaZn_{13}$ particles in Zn-0.3Ca alloy from 65 μm in as-cast state to 2 μm in as-rolled state. In the meantime, Zn grains are also refined from 352 μm to 1.4 μm. Elongation of the alloy reaches 49 %, which is the highest among Ca-containing Zn alloys.
(2) $CaZn_{13}$ serves as cathode in $CaZn_{13}$-Zn micro-galvanic cell. The refinement of $CaZn_{13}$ particles greatly suppresses pitting and improves corrosion uniformity. A calculation method is proposed to estimate initially released amount of Ca^{2+} ions by number of $CaZn_{13}$ particles.
(3) Ca^{2+} ions not only exhibit antibacterial activity against *E. coli* and *S. aureus*, but also promote MC3T3-E1 cell growth. The increased release proportion of Ca^{2+} ions is realized by refining $CaZn_{13}$ particles, which breaks the trade-off between antibacterial ability and biocompatibility.
(4) The BCWC-rolled alloy shows good osteogenic differentiation ability *in vitro*, which shows potential for making GBR membranes.

Ethics approval and consent to participate

We can confirm that this manuscript has not been involved any ethical issues as we did not carried out any human or animal experiments and did not collect any personal information or sensitive data.

Data availability statement

The raw data can be shared on requirement.

CRediT authorship contribution statement

Xiang-Min Li: Writing – original draft, Methodology, Investigation, Formal analysis, Data curation, Conceptualization. **Zhang-Zhi Shi:** Writing – review & editing, Supervision, Resources, Project administration, Methodology, Funding acquisition, Conceptualization. **Ayisulu Tuoliken:** Methodology, Investigation. **Wei Gou:** Formal analysis. **Chang-Heng Li:** Investigation. **Lu-Ning Wang:** Writing – review & editing, Supervision, Resources, Project administration, Methodology, Funding acquisition, Conceptualization.

Declaration of competing interest

Lu-Ning Wang is an editorial board member for Bioactive Materials was not involved in the editorial review or the decision to publish this paper. The authors declare that they have no known competing financial interests or personal relationships that could have appeared to influence the work reported in this paper.

Acknowledgement

This work is financially supported by Xiongan New Area Science and Technology Innovation Project(2022XACX0600), the National Natural Science Foundation of China (No. 52231010 and No. 52071028) and Beijing Nova Program (2022 Beijing Nova Program Cross Cooperation Program No. 20220484178).

Appendix A. Supplementary data

Supplementary data to this article can be found online at https://doi.org/10.1016/j.bioactmat.2024.08.049.

References

[1] I. Elgali, A. Turri, W. Xia, B. Norlindh, A. Johansson, C. Dahlin, P. Thomsen, O. Omar, Guided bone regeneration using resorbable membrane and different bone substitutes: early histological and molecular events, Acta Biomater. 29 (2016) 409–423.
[2] H.N. Woo, Y.J. Cho, S. Tarafder, C.H. Lee, The recent advances in scaffolds for integrated periodontal regeneration, Bioact. Mater. 6 (2021) 3328–3342.
[3] J.T. Kalitheertha Thevar, N.A.N. Nik Malek, M.R. Abdul Kadir, In vitro degradation of triple layered poly (lactic-co-glycolic acid) composite membrane composed of nanoapatite and lauric acid for guided bone regeneration applications, Mater. Chem. Phys. 221 (2019) 501–514.
[4] S.Y. Cheon, J. Kim, K.Y. Lee, C.M. Lee, Poly (l-lactic acid) membrane crosslinked with Genipin for guided bone regeneration, Int. J. Biol. Macromol. 191 (2021) 1228–1239.
[5] W. Zhang, P. Li, G. Shen, X. Mo, C. Zhou, D. Alexander, F. Rupp, J. Geis-Gerstorfer, H. Zhang, G. Wan, Appropriately adapted properties of hot-extruded Zn–0.5Cu–xFe alloys aimed for biodegradable guided bone regeneration membrane application, Bioact. Mater. 6 (2021) 975–989.
[6] Y.D. Rakhmatia, Y. Ayukawa, A. Furuhashi, K. Koyano, Current barrier membranes: titanium mesh and other membranes for guided bone regeneration in dental applications, J. Prosthodont. Res. 57 (2013) 3–14.
[7] T. Wu, L. Huang, J. Sun, J. Sun, Q. Yan, B. Duan, L. Zhang, B. Shi, Multifunctional chitin-based barrier membrane with antibacterial and osteogenic activities for the treatment of periodontal disease, Carbohydr. Polym. 269 (2021), 118276-1-10.
[8] X. Liu, X. He, D. Jin, S. Wu, H. Wang, M. Yin, A. Aldalbahi, M. El-Newehy, X. Mo, J. Wu, A biodegradable multifunctional nanofibrous membrane for periodontal tissue regeneration, Acta Biomater. 108 (2020) 207–222.
[9] C. Castellani, R.A. Lindtner, P. Hausbrandt, E. Tschegg, S.E. Stanzl-Tschegg, G. Zanoni, S. Beck, A.-M. Weinberg, Bone–implant interface strength and osseointegration: biodegradable magnesium alloy versus standard titanium control, Acta Biomater. 7 (2011) 432–440.
[10] M. Abdel-Hady Gepreel, M. Niinomi, Biocompatibility of Ti-alloys for long-term implantation, J. Mech. Behav. Biomed. Mater. 20 (2013) 407–415.
[11] J.K. Park, J. Yeom, E.J. Oh, M. Reddy, J.Y. Kim, D.-W. Cho, H.P. Lim, N.S. Kim, S. W. Park, H.I. Shin, D.J. Yang, K.B. Park, S.K. Hahn, Guided bone regeneration by poly(lactic-co-glycolic acid) grafted hyaluronic acid bi-layer films for periodontal barrier applications, Acta Biomater. 5 (2009) 3394–3403.

[12] E.S. Zhang, C.S. Zhu, J. Yang, H. Sun, X.M. Zhang, S.H. Li, Y.L. Wang, L. Sun, F. L. Yao, Electrospun PDLLA/PLGA composite membranes for potential application in guided tissue regeneration, Mater. Sci. Eng. C 58 (2016) 278–285.
[13] A.C. van Leeuwen, J.J.R. Huddleston Slater, P.F.M. Gielkens, J.R. de Jong, D. W. Grijpma, R.R.M. Bos, Guided bone regeneration in rat mandibular defects using resorbable poly(trimethylene carbonate) barrier membranes, Acta Biomater. 8 (2012) 1422–1429.
[14] Z. Shu, C. Zhang, L. Yan, H. Lei, C. Peng, S. Liu, L. Fan, Y. Chu, Antibacterial and osteoconductive polycaprolactone/polylactic acid/nano-hydroxyapatite/Cu@ZIF-8 GBR membrane with asymmetric porous structure, Int. J. Biol. Macromol. 224 (2023) 1040–1051.
[15] D.D. Xia, F. Yang, Y.F. Zheng, Y.S. Liu, Y.S. Zhou, Research status of biodegradable metals designed for oral and maxillofacial applications: a review, Bioact. Mater. 6 (2021) 4186–4208.
[16] P.K. Bowen, J. Drelich, J. Goldman, Zinc exhibits ideal physiological corrosion behavior for bioabsorbable stents, Adv. Mater. 25 (2013) 2577–2582.
[17] H. Guo, D.D. Xia, Y.F. Zheng, Y. Zhu, Y.S. Liu, Y.S. Zhou, A pure zinc membrane with degradability and osteogenesis promotion for guided bone regeneration: in vitro and in vivo studies, Acta Biomater. 106 (2020) 396–409.
[18] Y.C. Su, K. Wang, J.L. Gao, Y. Yang, Y.X. Qin, Y.F. Zheng, D.H. Zhu, Enhanced cytocompatibility and antibacterial property of zinc phosphate coating on biodegradable zinc materials, Acta Biomater. 98 (2019) 174–185.
[19] D.A. Robinson, R.W. Griffith, D. Shechtman, R.B. Evans, M.G. Conzemius, In vitro antibacterial properties of magnesium metal against Escherichia coli, Pseudomonas aeruginosa and Staphylococcus aureus, Acta Biomater. 6 (2010) 1869–1877.
[20] G.D. Jin, H.L. Cao, Y.Q. Qiao, F.H. Meng, H.Q. Zhu, X.Y. Liu, Osteogenic activity and antibacterial effect of zinc ion implanted titanium, Colloids Surf., B 117 (2014) 158–165.
[21] Y.W. Wang, A. Cao, Y. Jiang, X. Zhang, J.H. Liu, Y.F. Liu, H.F. Wang, Superior antibacterial activity of zinc oxide/graphene oxide composites originating from high zinc concentration localized around bacteria, ACS Appl. Mater. Interfaces 6 (2014) 2791–2798.
[22] J. Ma, N. Zhao, D.H. Zhu, Bioabsorbable zinc ion induced biphasic cellular responses in vascular smooth muscle cells, Sci. Rep. 6 (2016), 26661-1-10.
[23] E.R. Shearier, P.K. Bowen, W. He, A. Drelich, J. Drelich, J. Goldman, F. Zhao, In vitro cytotoxicity, adhesion, and proliferation of human vascular cells exposed to zinc, ACS Biomater. Sci. Eng. 2 (2016) 634–642.
[24] J. Ma, N. Zhao, D. Zhu, Endothelial cellular responses to biodegradable metal zinc, ACS Biomater. Sci. Eng. 1 (2015) 1174–1182.
[25] A. Ito, H. Kawamura, M. Otsuka, M. Ikeuchi, H. Ohgushi, K. Onuma, N. Kanzaki, Y. Sogo, N. Ichinose, Zinc-releasing calcium phosphate for stimulating bone formation, Mater. Sci. Eng. C 22 (2002) 21–25.
[26] H.T. Yang, B. Jia, Z.C. Zhang, X.H. Qu, G.N. Li, W.J. Lin, D.H. Zhu, K.R. Dai, Y. F. Zheng, Alloying design of biodegradable zinc as promising bone implants for load-bearing applications, Nat. Commun. 11 (2020), 401-1-16.
[27] N. Yang, N. Balasubramani, J. Venezuela, S. Almathami, C.E. Wen, M. Dargusch, The influence of Ca and Cu additions on the microstructure, mechanical and degradation properties of Zn–Ca–Cu alloys for absorbable wound closure device applications, Bioact. Mater. 6 (2021) 1436–1451.
[28] Z.C. Zhang, B. Jia, H.T. Yang, Y. Han, Q. Wu, K.R. Dai, Y.F. Zheng, Biodegradable ZnLiCa ternary alloys for critical-sized bone defect regeneration at load-bearing sites: in vitro and in vivo studies, Bioact. Mater. 6 (2021) 3999–4013.
[29] H.F. Li, X.H. Xie, Y.F. Zheng, Y. Cong, F.Y. Zhou, K.J. Qiu, X. Wang, S.H. Chen, L. Huang, L. Tian, L. Qin, Development of biodegradable Zn-1X binary alloys with nutrient alloying elements Mg, Ca and Sr, Sci. Rep. 5 (2015), 10719-1-14.
[30] Y.L. Zou, X. Chen, B. Chen, Effects of Ca concentration on degradation behavior of Zn-x Ca alloys in Hank's solution, Mater. Lett. 218 (2018) 193–196.
[31] Z.Z. Shi, X.X. Gao, H.J. Zhang, X.F. Liu, H.Y. Li, C. Zhou, Y.X. Yin, L.N. Wang, Design biodegradable Zn alloys: second phases and their significant influences on alloy properties, Bioact. Mater. 5 (2020) 210–218.
[32] H.F. Li, H.T. Yang, Y.F. Zheng, F.Y. Zhou, K.J. Qiu, X. Wang, Design and characterizations of novel biodegradable ternary Zn-based alloys with IIA nutrient alloying elements Mg, Ca and Sr, Mater. Des. 83 (2015) 95–102.
[33] Z.Z. Shi, H.Y. Li, J.Y. Xu, X.X. Gao, X.F. Liu, Microstructure evolution of a high-strength low-alloy Zn–Mn–Ca alloy through casting, hot extrusion and warm caliber rolling, Mater. Sci. Eng. 771 (2020), 136626-1-11.
[34] N. Yang, N. Balasubramani, J. Venezuela, H. Bielefeldt-Ohmann, R. Allavena, S. Almathami, M. Dargusch, Microstructure refinement in biodegradable Zn-Cu-Ca alloy for enhanced mechanical properties, degradation homogeneity, and strength retention in simulated physiological condition, J. Mater. Sci. Technol. 125 (2022) 1–14.
[35] Z. Li, Z.Z. Shi, H.J. Zhang, H.F. Li, Y. Feng, L.N. Wang, Hierarchical microstructure and two-stage corrosion behavior of a high-performance near-eutectic Zn-Li alloy, J. Mater. Sci. Technol. 80 (2021) 50–65.
[36] J.X. Lin, X. Tong, Z.M. Shi, D.C. Zhang, L.S. Zhang, K. Wang, A.P. Wei, L.F. Jin, J. G. Lin, Y.C. Li, C.E. Wen, A biodegradable Zn-1Cu-0.1Ti alloy with antibacterial properties for orthopedic applications, Acta Biomater. 106 (2020) 410–427.
[37] Z.Z. Shi, X.M. Li, S.L. Yao, Y.Z. Tang, X.J. Ji, Q. Wang, X.X. Gao, L.N. Wang, 300 MPa grade biodegradable high-strength ductile low-alloy (BHSDLA) Zn-Mn-Mg alloys: an in vitro study, J. Mater. Sci. Technol. 138 (2023) 233–244.
[38] P. Rider, Ž.P. Kačarević, A. Elad, D. Tadic, D. Rothamel, G. Sauer, F. Bornert, P. Windisch, D.B. Hangyási, B. Molnar, E. Bortel, B. Hesse, F. Witte, Biodegradable magnesium barrier membrane used for guided bone regeneration in dental surgery, Bioact. Mater. 14 (2022) 152–168.
[39] H.T. Chen, Z.Z. Shi, X.F. Liu, Microstructure and mechanical properties of extruded and caliber rolled biodegradable Zn-0.8Mn-0.4Ag alloy with high ductility, Mater. Sci. Eng. 770 (2020), 138543-1-11.
[40] Z.Z. Shi, M. Li, X.M. Li, L.N. Wang, Surface-roughness-induced plasticity in a biodegradable Zn alloy, Adv. Mater. 35 (2022), 2207570-2207571-12.
[41] C.D. Barrett, A. Imandoust, A.L. Oppedal, K. Inal, M.A. Tschopp, H. El Kadiri, Effect of grain boundaries on texture formation during dynamic recrystallization of magnesium alloys, Acta Mater. 128 (2017) 270–283.
[42] M. Leonard, C. Moussa, A. Roatta, A. Seret, J.W. Signorelli, Continuous dynamic recrystallization in a Zn–Cu–Ti sheet subjected to bilinear tensile strain, Mater. Sci. Eng. 789 (2020), 139689-1-11.
[43] L.Y. Han, Y.N. Yu, D.J. Wei, X. Wang, G.Q. Zhao, G.C. Wang, The synergistic and interactive effects of slip systems and dynamic recrystallization on the weakening basal texture of Mg-Y-Nd-Zr-Gd magnesium alloy, Mater. Des. 237 (2024), 112583-1-13.
[44] W. Jiang, X. Ren, L. Yu, J. Sun, S. Ni, Y. Huang, M. Song, Twinning-assisted static recrystallization and texture evolution in a Mg-Gd-Y-Zr alloy, J. Mater. Res. Technol. 28 (2024) 4250–4261.
[45] J. Pinc, A. Školáková, P. Veřtát, J. Duchoň, J. Kubásek, P. Lejček, D. Vojtěch, J. Čapek, Microstructure evolution and mechanical performance of ternary Zn-0.8Mg-0.2Sr (wt. %) alloy processed by equal-channel angular pressing, Mater. Sci. Eng. 824 (2021), 141809-1-14.
[46] V. Hybasek, J. Kubasek, J. Capek, D. Alferi, J. Pinc, J. Jiru, J. Fojt, Influence of model environment complexity on corrosion mechanism of biodegradable zinc alloys, Corrosion Sci. 187 (2021), 109520-109521-12.
[47] B.Y. Li, Z.Z. Shi, W.-B. Geng, Y. Yan, L.N. Wang, Effect of bovine serum albumin on immersion corrosion and tribocorrosion behavior of Zn-0.4Mn alloy in simulated body fluid, Corrosion Sci. 235 (2024), 112165-1-20.
[48] G. Ballerini, K. Ogle, M.G. Barthés-Labrousse, The acid–base properties of the surface of native zinc oxide layers: an XPS study of adsorption of 1,2-diaminoethane, Appl. Surf. Sci. 253 (2007) 6860–6867.
[49] J. Duchoslav, R. Steinberger, M. Arndt, T. Keppert, G. Luckeneder, K. H. Stellnberger, J. Hagler, G. Angeli, C.K. Riener, D. Stifter, Evolution of the surface chemistry of hot dip galvanized Zn–Mg–Al and Zn coatings on steel during short term exposure to sodium chloride containing environments, Corrosion Sci. 91 (2015) 311–320.
[50] Y. Meng, L. Liu, D. Zhang, C. Dong, Y. Yan, A.A. Volinsky, L.-N. Wang, Initial formation of corrosion products on pure zinc in saline solution, Bioact. Mater. 4 (2019) 87–96.
[51] X. Liu, H.T. Yang, P. Xiong, W.T. Li, H.H. Huang, Y.F. Zheng, Comparative studies of Tris-HCl, HEPES and NaHCO3/CO2 buffer systems on the biodegradation behaviour of pure Zn in NaCl and SBF solutions, Corrosion Sci. 157 (2019) 205–219.
[52] S.Y. Huang, H. Liu, Y.J. Su, L.J. Qiao, Y. Yan, Significant influence of trace Li on the mechanical properties, corrosion behavior, and antibacterial properties of biodegradable Zn–4Cu alloys, J. Mater. Sci. Technol. 151 (2023) 245–257.
[53] M. Wątroba, K. Mech, W. Bednarczyk, J. Kawałko, M. Marciszko-Wiąckowska, M. Marzec, D.E.T. Shepherd, P. Bała, Long-term in vitro corrosion behavior of Zn-3Ag and Zn-3Ag-0.5Mg alloys considered for biodegradable implant applications, Mater. Des. 213 (2022), 110289-1-18.
[54] L. Li, H.Z. Jiao, C.F. Liu, L. Yang, Y.S. Suo, R.X. Zhang, T. Liu, J.Z. Cui, Microstructures, mechanical properties and in vitro corrosion behavior of biodegradable Zn alloys microalloyed with Al, Mn, Cu, Ag and Li elements, J. Mater. Sci. Technol. 103 (2022) 244–260.
[55] J.L. Sun, Y. Feng, Z.Z. Shi, Z. Xue, M. Cao, S.L. Yao, Z. Li, L.N. Wang, Biodegradable Zn-0.5Li alloy rib plate: processing procedure development and in vitro performance evaluation, J. Mater. Sci. Technol. 141 (2023) 245–256.
[56] X. Tong, Z.M. Shi, L.C. Xu, J.X. Lin, D.C. Zhang, K. Wang, Y.C. Li, C.E. Wen, Degradation behavior, cytotoxicity, hemolysis, and antibacterial properties of electro-deposited Zn–Cu metal foams as potential biodegradable bone implants, Acta Biomater. 102 (2020) 481–492.
[57] J.X. Lin, X. Tong, K. Wang, Z.M. Shi, Y.C. Li, M. Dargusch, C.E. Wen, Biodegradable Zn–3Cu and Zn–3Cu–0.2Ti alloys with ultrahigh ductility and antibacterial ability for orthopedic applications, J. Mater. Sci. Technol. 68 (2021) 76–90.
[58] X. Tong, L. Zhu, Y.H. Wu, Y.T. Song, K. Wang, S.B. Huang, Y.C. Li, J.F. Ma, C. E. Wen, J.X. Lin, A biodegradable Fe/Zn–3Cu composite with requisite properties for orthopedic applications, Acta Biomater. 146 (2022) 506–521.
[59] X. Tong, T.X. Shen, X. Zhou, J. Zeng, J.Y. Tao, K. Munir, Y.C. Li, S.B. Huang, X. H. Wu, J.F. Ma, J.X. Lin, C.E. Wen, Biodegradable Zn–Cu–Li alloys with ultrahigh strength, ductility, antibacterial ability, cytocompatibility, and suitable degradation rate for potential bone-implant applications, Smart Mater. Manufact. 1 (2023), 100012-1-14.
[60] H.R. Bakhsheshi-Rad, E. Hamzah, H.T. Low, M. Kasiri-Asgarani, S. Farahany, E. Akbari, M.H. Cho, Fabrication of biodegradable Zn-Al-Mg alloy: mechanical properties, corrosion behavior, cytotoxicity and antibacterial activities, Mater. Sci. Eng. C 73 (2017) 215–219.
[61] L. Zhu, X. Tong, Z.Q. Ye, Z.Q. Lin, T.H. Zhou, S.B. Huang, Y.C. Li, J.X. Lin, C. E. Wen, J.F. Ma, Zinc phosphate, zinc oxide, and their dual-phase coatings on pure Zn foam with good corrosion resistance, cytocompatibility, and antibacterial ability for potential biodegradable bone-implant applications, Chem. Eng. J. 450 (2022), 137946-1-16.
[62] X. Tong, Y. Han, R.Q. Zhou, W.Y. Jiang, L. Zhu, Y.C. Li, S.B. Huang, J.F. Ma, C. E. Wen, J.X. Lin, Biodegradable Zn–Dy binary alloys with high strength, ductility, cytocompatibility, and antibacterial ability for bone-implant applications, Acta Biomater. 155 (2023) 684–702.

[63] X. Tong, Y. Han, R.Q. Zhou, J. Zeng, C. Wang, Y.F. Yuan, L. Zhu, S.B. Huang, J. F. Ma, Y.C. Li, C.E. Wen, J.X. Lin, Mechanical properties, corrosion and degradation behaviors, and in vitro cytocompatibility of a biodegradable Zn–5La alloy for bone-implant applications, Acta Biomater. 169 (2023) 641–660.
[64] H. Huang, H. Liu, L.S. Wang, K. Yan, Y.H. Li, J.H. Jiang, A.B. Ma, F. Xue, J. Bai, Revealing the effect of minor Ca and Sr additions on microstructure evolution and mechanical properties of Zn-0.6 Mg alloy during multi-pass equal channel angular pressing, J. Alloys Compd. 844 (2020), 155923-1-11.
[65] Z.Z. Shi, J. Yu, X.F. Liu, H.J. Zhang, D.W. Zhang, Y.-X. Yin, L.N. Wang, Effects of Ag, Cu or Ca addition on microstructure and comprehensive properties of biodegradable Zn-0.8Mn alloy, Mater. Sci. Eng. C 99 (2019) 969–978.
[66] X.W. Liu, J.K. Sun, K.J. Qiu, Y.H. Yang, Z.J. Pu, L. Li, Y.F. Zheng, Effects of alloying elements (Ca and Sr) on microstructure, mechanical property and in vitro corrosion behavior of biodegradable Zn–1.5Mg alloy, J. Alloys Compd. 664 (2016) 444–452.
[67] Q.L. Li, M. Wei, J. Yang, Z.X. Zhao, J.Q. Ma, D.X. Liu, Y.F. Lan, Effect of Ca addition on the microstructure, mechanical properties and corrosion rate of degradable Zn-1Mg alloys, J. Alloys Compd. 887 (2021), 161255-1-11.
[68] O. Avior, N.B. Ghedalia-Peled, T. Ron, R. Vago, E. Aghion, The effect of Ca on in vitro behavior of biodegradable Zn-Fe alloy in simulated physiological environments, Metals 10 (2020), 1624-1-14.
[69] Z.Z. Shi, J. Yu, Z.K. Ji, X.F. Liu, X.F. Gu, G. Han, Influence of solution heat treatment on microstructure and hardness of as-cast biodegradable Zn–Mn alloys, J. Mater. Sci. 54 (2018) 1728–1740.
[70] H.L. Wu, C.J. Zhang, T.F. Lou, B.W. Chen, R.B. Yi, W.H. Wang, R.P. Zhang, M. C. Zuo, H.D. Xu, P. Han, S.X. Zhang, J.H. Ni, X.N. Zhang, Crevice corrosion – a newly observed mechanism of degradation in biomedical magnesium, Acta Biomater. 98 (2019) 152–159.
[71] B.W. Chen, H.L. Wu, R.B. Yi, W.H. Wang, H.D. Xu, S.X. Zhang, H.Z. Peng, J.W. Ma, H.M. Jiang, R. Zan, S. Qiao, Y. Sun, P. Hou, P. Han, J.H. Ni, X.N. Zhang, In vitro crevice corrosion of biodegradable magnesium in different solutions, J. Mater. Sci. Technol. 52 (2020) 83–88.
[72] S.Y. Huang, W. Wu, Y.J. Su, L.J. Qiao, Y. Yan, Insight into the corrosion behaviour and degradation mechanism of pure zinc in simulated body fluid, Corrosion Sci. 178 (2021), 109071-1-12.
[73] L.J. Liu, Y. Meng, C.F. Dong, Y. Yan, A.A. Volinsky, L.N. Wang, Initial formation of corrosion products on pure zinc in simulated body fluid, J. Mater. Sci. Technol. 34 (2018) 2271–2282.
[74] S. Samani, S.M. Hossainalipour, M. Tamizifar, H.R. Rezaie, In vitroantibacterial evaluation of sol-gel-derived Zn-, Ag-, and (Zn + Ag)-doped hydroxyapatite coatings against methicillin-resistantStaphylococcus aureus, J. Biomed. Mater. Res. A. 101A (2013) 222–230.
[75] C.Y. Ning, X.L. Wang, L.H. Li, Y. Zhu, M. Li, P. Yu, L. Zhou, Z.N. Zhou, J.Q. Chen, G. X. Tan, Y. Zhang, Y.J. Wang, C.B. Mao, Concentration ranges of antibacterial cations for showing the highest antibacterial efficacy but the least cytotoxicity against mammalian cells: implications for a New antibacterial mechanism, Chem. Res. Toxicol. 28 (2015) 1815–1822.
[76] J. Pasquet, Y. Chevalier, J. Pelletier, E. Couval, D. Bouvier, M.A. Bolzinger, The contribution of zinc ions to the antimicrobial activity of zinc oxide, Colloids Surf. A Physicochem. Eng. Asp. 457 (2014) 263–274.
[77] B.B. Wang, Y.C. Li, S.S. Wang, F.H. Jia, A.Q. Bian, K. Wang, L. Xie, K. Yan, H. X. Qiao, H. Lin, J.P. Lan, Y. Huang, Electrodeposited dopamine/strontium-doped hydroxyapatite composite coating on pure zinc for anti-corrosion, antimicrobial and osteogenesis, Mater. Sci. Eng. C 129 (2021), 112387-1-14.
[78] B.L. Tao, M.W. Chen, C.C. Lin, L. Lu, Z. Yuan, J. Liu, Q. Liao, Z. Xia, Z.H. Peng, K. Y. Cai, Zn-incorporation with graphene oxide on Ti substrates surface to improve osteogenic activity and inhibit bacterial adhesion, J. Biomed. Mater. Res. A. 107 (2019) 2310–2326.
[79] X.M. Ji, M.L. Zhao, L. Dong, X. Han, D.J. Li, Influence of Ag/Ca ratio on the osteoblast growth and antibacterial activity of TiN coatings on Ti-6Al-4V by Ag and Ca ion implantation, Surf. Coat. Technol. 403 (2020), 126415-1-9.
[80] M.L. Zhao, X.M. Ji, D.J. Li, Ag+ and Ca+ single implantation and co-implantation induced the cell growth and antibacterial activity of TiN/Ti-6Al-4V, Vacuum 207 (2023), 111579-1-7.
[81] J.L. Wang, F. Witte, T.F. Xi, Y.F. Zheng, K. Yang, Y.S. Yang, D.W. Zhao, J. Meng, Y. D. Li, W.R. Li, K.M. Chan, L. Qin, Recommendation for modifying current cytotoxicity testing standards for biodegradable magnesium-based materials, Acta Biomater. 21 (2015) 237–249.
[82] P. Habibovic, J.E. Barralet, Bioinorganics and biomaterials: bone repair, Acta Biomater. 7 (2011) 3013–3026.
[83] Y. Ma, D. Ran, H. Zhao, X. Shi, R. Song, H. Zou, Z. Liu, The effect of P2X7R-mediated Ca^{2+} and MAPK signaling in OPG-induced duck embryo osteoclasts differentiation and adhesive structure damage, Life Sci. 293 (2022), 120337-1-9.
[84] C.B.S.S. Danoux, D.C. Bassett, Z. Othman, A.I. Rodrigues, R.L. Reis, J.E. Barralet, C. A. van Blitterswijk, P. Habibovic, Elucidating the individual effects of calcium and phosphate ions on hMSCs by using composite materials, Acta Biomater. 17 (2015) 1–15.
[85] V.A. Romanova, R.R. Balokhonov, S. Schmauder, The influence of the reinforcing particle shape and interface strength on the fracture behavior of a metal matrix composite, Acta Mater. 57 (2009) 97–107.
[86] L. Gu, A. Meng, X. Chen, Y.H. Zhao, Simultaneously enhancing strength and ductility of HCP titanium via multi-modal grain induced extra <c+a> dislocation hardening, Acta Mater. 252 (2023), 118949-1-15.
[87] Z.Z. Shi, J. Yu, X.F. Liu, Microalloyed Zn-Mn alloys: from extremely brittle to extraordinarily ductile at room temperature, Mater. Des. 144 (2018) 343–352.
[88] W. Bednarczyk, J. Kawałko, M. Wątroba, P. Bała, Achieving room temperature superplasticity in the Zn-0.5Cu alloy processed via equal channel angular pressing, Mater. Sci. Eng. 723 (2018) 126–133.
[89] M. Li, Z.Z. Shi, Q. Wang, Y. Cheng, L.N. Wang, Zn–0.8Mn alloy for degradable structural applications: hot compression behaviors, four dynamic recrystallization mechanisms, and better elevated-temperature strength, J. Mater. Sci. Technol. 137 (2023) 159–175.
[90] J.J. He, Y. Mao, Y.J. Fu, B. Jiang, K. Xiong, S.M. Zhang, F.S. Pan, Improving the room-temperature formability of Mg-3Al-1Zn alloy sheet by introducing an orthogonal four-peak texture, J. Alloys Compd. 797 (2019) 443–455.
[91] Y.N. Wang, J.C. Huang, Texture analysis in hexagonal materials, Mater. Chem. Phys. 81 (2003) 11–26.
[92] R.M. Li, Y.T. Ding, H.F. Zhang, J. Lei, Y. Shen, Effective strengthening and toughening in Zn–1Mg alloy with bimodal grain structure achieved by conventional extrusion, Mater. Sci. Eng. 854 (2022) 143850–143851, 12.
[93] J. Luo, W.W. Hu, Q.Q. Jin, H. Yan, R.S. Chen, Unusual cold rolled texture in an Mg-2.0Zn-0.8Gd sheet, Scripta Mater. 127 (2017) 146–150.
[94] G.G. Wang, G.S. Huang, X. Chen, Q.Y. Deng, A.T. Tang, B. Jiang, F.S. Pan, Effects of Zn addition on the mechanical properties and texture of extruded Mg-Zn-Ca-Ce magnesium alloy sheets, Mater. Sci. Eng. 705 (2017) 46–54.
[95] Q.H. Wang, Y.Q. Shen, B. Jiang, A.T. Tang, J.F. Song, Z.T. Jiang, T.H. Yang, G. S. Huang, F.S. Pan, A micro-alloyed Mg-Sn-Y alloy with high ductility at room temperature, Mater. Sci. Eng. 735 (2018) 131–144.
[96] D. Liu, Z.Y. Liu, E. Wang, Effect of rolling reduction on microstructure, texture, mechanical properties and mechanical anisotropy of AZ31 magnesium alloys, Mater. Sci. Eng. 612 (2014) 208–213.